Plasmonic topological metasurface by encircling an exceptional point.

— Source link ⤢

Qinghua Song, Mutasem Odeh, Jesús Zúñiga-Pérez, Boubacar Kante ...+2 more authors

Institutions: Centre national de la recherche scientifique, University of California, Berkeley, Lawrence Berkeley National Laboratory

Topics: Phase (waves)

Related papers:

- Plasmonic and Dielectric Metasurfaces: Design, Fabrication and Applications

- Ultrathin metasurface with topological transition for manipulating spoof surface plasmon polaritons

- Ultrathin metalens and three-dimensional optical holography using metasurfaces

- Exceptional point-based plasmonic metasurfaces for vortex beam generation.

- Nonreciprocal Asymmetric Polarization Encryption by Layered Plasmonic Metasurfaces.

Share this paper: 𝗳 𝕏 in ✉

View more about this paper here: https://typeset.io/papers/plasmonic-topological-metasurface-by-encircling-an-oinsbggr6t

Title: Plasmonic Topological Metasurface by Encircling an Exceptional Point

Short title: Exceptional Topological Metasurface

Authors: Qinghua Song[1], Mutasem Odeh[2], Jesús Zúñiga-Pérez[1], Boubacar Kanté[2], and Patrice Genevet[1]*

Affiliations:

[1]Université Côte d'Azur, CNRS, CRHEA, Rue Bernard Gregory, Sophia Antipolis 06560 Valbonne, France

[2]Depertment of Electrical Engineering and Computer Sciences, University of California, Berkeley, CA 94720, USA

*Correspondence to: Patrice.Genevet@crhea.cnrs.fr.

Abstract: Resonant scattering, guided mode propagation phase and/or orientation-dependent phase retardations are the three main mechanisms used until now to conceive optical metasurfaces. Here we introduce an additional degree of freedom to address optical phase engineering by exploiting the topological features of non-Hermitian matrices operating near their singular points. Choosing metasurface building blocks to encircle a singularity following an arbitrarily closed trajectory in parameter space, we engineer topologically-protected full $2\pi -$ phase on a specific reflected polarization channel. The ease of implementation together with its compatibility with other phase-addressing mechanisms bring topological properties into the realm of industrial applications at optical frequencies, and prove that metasurface technology represents a convenient test bench to study and validate topological photonic concepts.

One Sentence Summary: Topology-protected 2π phase by encircling exceptional point in arbitrary closed path for unique metasurface wavefront shaping.

Metasurfaces (*1–6*) are artificial materials constructed with subwavelength arrays of spatially-distributed nanostructures that enable versatile wave front engineering. From a fundamental perspective, a metasurface is an open system, continuously exchanging and/or absorbing energy between the impinging field and the resonant nanostructures. Unlike closed systems, open systems experience a phase transition at the exceptional point (EP) leading to complex scattering phenomena related to optical singularities (*7*). The latter can be equivalently described in an optical system using the scattering matrix and Hamiltonian representations (*8–10*). Singularities also manifest in the reflection-zero regime, perfect absorption and bound state in the continuum, giving rise to unidirectional transmission or reflection (*11*, *12*), single mode laser operation (*13*), extreme sensitiveness to perturbation (*14*, *15*), etc. Tailoring light reflection, or transmission, with metasurfaces consists in addressing the values of complex coefficients by varying the nanostructure geometries. Choosing any arbitrary loop in parameter space to achieve phase distribution does not necessarily lead to full 2π phase accumulation. Here we show how to leverage on the 2π-phase excursion occurring on the coefficient value by encircling zeros/singularities in the complex plane. Encircling singular point to accumulate an optical phase difference is of crucial interest for wavefront engineering, enrichening the metasurface design toolbox with an additional phase addressing mechanism.

Previous works on metasurfaces have shown that non-Hermitian metasurfaces can operate close to an EP, and have approached the singularity thanks to a series of individually-distinct metasurfaces for which a given parameter is changed (*16–19*). The exploitation of the robust topological phase around the EP, referred to as exceptional topological (ET) phase, to realize functional devices has remained elusive. The proposed ET-phase is fundamentally different from conventional Pancharatnam-Berry (PB) phase (*20–23*) and, as a consequence, ET can be combined with other phase addressing mechanisms, including PB, to achieve full and independent control of the polarization channels. We demonstrate a meta-hologram using the ET phase encircling the EP to project an image of "C" for left circular polarized (LCP) light, leaving the cross right circular polarized (RCP) channel unaffected. By combining the ET and PB phases, we decouple the two circular polarizations (CP) and achieve two different holographic projections with an image of "A" for LCP light and "B" for RCP light.

The plasmonic topological metasurface consists of three layers, where a dielectric layer is sandwiched between a metal ground and a metallic structured layer, as shown in Fig. 1A. The

metal ground blocks all the transmission so that the metasurface works in the reflective regime. The structured layer is formed by a two-dimensional (2D) planar chiral structure array, which is composed of an "L" shaped nanostructure, near-field coupled to a straight nano rod, representing a Hangul syllable of "ㅡ". To observe the EP complex-square-root topology of the eigenvalues surface, two parameters need to be varied, defining thereby the parameter space $\boldsymbol{R} = (L_1, L_3)$, with L_1 and L_3 being the geometrical parameters shown in Fig. 1A. L_1 and L_3 are chosen as they play key roles in the y- and x-polarized resonances, as shown in Supplementary fig. S9 and Note 4, giving access to a full 2π reflection phase for r_{+-} (where the subscript $+-$ represent reflected CP conversion from RCP ($|-\rangle$) to LCP ($|+\rangle$)). The EP is obtained by adjusting the nanostructure structural properties, so that both eigenstates degenerate as CP beams. If the degenerate eigenstate is RCP, i.e., $\hat{r}|-\rangle = \lambda_{1,2}|-\rangle$, where $\hat{r}$ is the reflection matrix and $\lambda_1 = \lambda_2$ are two degenerate eigenvalues, then RCP input light is preserved, and the CP conversion channel from RCP to LCP vanishes, i.e., $r_{+-} = 0$. A zero point or singularity point, equivalent to perfect absorption cases (24–26), is obtained for r_{+-} as shown in Fig. 1B. The chiral response of the surface current distribution at the EP, shown in the Supplementary fig. S7, is a key ingredient to achieve circular polarization dependent reflectivity. The induced chirality is an inherent property of the EP from a symmetric non-Hermitian Hamiltonian (27) and leads to an asymmetric conversion from one circular polarization to the other and vice versa (i.e., $r_{+-} \neq r_{-+}$). Interestingly, the spectral response of only one of the two CP conversion undergoes a 2π phase change around the EP wavelength. Due to the topological protection provided by encircling of the EP, as discussed in Supplementary Note 1 and 2, the 2π phase accumulation is maintained for the reflected phase map irrespective of the closed path, as long as it encircles one EP in parameter space. Given the metasurface versatility, we realize on a single component an assembly of antennas with different parameters chosen so as to move around the EP in the parameter space, thus realizing simultaneously a set of optical responses (see Fig. 1G and 1J). Amplitude variation with singular value is also observed. The other reflective CP conversion coefficient (r_{-+}) does not present a singularity in this parameter space, resulting in an almost constant phase and amplitude profiles as shown in Fig. 1C.

The conventional PB phase works oppositely for the two reflective CP conversion beams, as reported in Fig. 1D-1F. Being fundamentally different, ET phase is imposed on only one CP

conversion and thus can be combined with the standard PB phase (see more details in Supplementary Note 5). As a result, the combination of ET and PB phases can be used to decouple the phase of the two CP conversion beams, leading to independent control of each polarization converted wavefront, as shown in Fig. 1G-1L.

A spectral singularity point of r_{+-}, together with its degeneracy of the eigenvalues and eigenstates at $\lambda = 600$ nm proof the existence of an EP as shown by the red star in Fig. 2. This behavior is further confirmed by the intersecting double Riemann surface corresponding to the reflection matrix eigenvalues as shown in Fig. 3A and 3B. Various phase and amplitude-conversion distribution choices are possible for the deflecting unit-cell. Here we chose a simple unit-cell phase coverage, i.e., considering $90°$ phase steps, so as to keep the distance between neighboring antennas constant, which slightly compromises the amplitude of the third structure as shown in Fig. 3E. Seven designs of PB phase interval of $60°$ are also presented in Fig. 3C-3H for the combination with ET phase.

We experimentally demonstrate an ET-phase gradient metasurface, behaving as a beam deflector and a meta-hologram. The scanning electron micrograph (SEM) of the fabricated beam deflector is shown in Fig. 4A. An asymmetric reflection of the two CP conversion beams is measured in Fig. 4B, with a maximum efficiency of 12% and power ratio around 10:1 as quantified in Fig. 4C. The spectral position of the singular design (EP antenna) evolves as a function of the antenna structural parameters, as shown in Fig. S13, indicating that small nanofabrication errors can slightly shift the position of the EP and modify the expected deflection efficiencies and power ratio. To show the versatility of this wavefront phase encoding technique we realize a meta-hologram as fabricated in Fig. 4D. As expected, a holographic image of "C" is displayed for r_{+-} as shown in Fig. 4E, but no image appears for r_{-+} as shown in Fig. 4F.

The wealth of applications of the ET phase expands by combining it with other phase-control mechanisms. Here, ET is combined with the widespread PB phase by simply rotating the metasurface elements, as shown in Fig. 4G-4L, to decouple the deflection angles of the two CP beams in Fig. 4H and 4I. Similarly, ET+PB phase encoding is applied to project two different CP holographic images as shown in Fig. 4K and 4L.

Concluding remarks. We have demonstrated a planar chiral plasmonic metasurface that exhibits 2π topological phase accumulation in reflection regime by choosing nanoantenna designs

distributed along any arbitrarily closed parameter loop encircling the EP. We have shown 2π-phase accumulation is imposed on only one of the CP conversion beams defined by the chirality of the encircled EP. Exploiting a linear combination of ET and PB phases we decoupled LCP and RCP channels. Addressing phase retardation by encircling singularities of the S-matrix open vast research opportunities for unusual polarization, linear and nonlinear topological electromagnetic field control at optical frequencies.

References and Notes:

1. N. Yu, et al., *Science*. **334**, 333–337 (2011).

2. P. Genevet, et al., *Nat. Nanotechn.* **10**, 804–809 (2015).

3. A. Alù, N. Engheta, *Nat. Photonics* **2**, 307–310 (2008).

4. Q. Song, et al., *Nat Commun*. **12**, 3631 (2021).

5. M. V. Gorkunov, A. A. Antonov, Y. S. Kivshar, *Phys. Rev. Lett.* **125**, 093903 (2020),

6. D. B. Haim, L. Michaeli, O. Avayu, T. Ellenbogen, *Opt. Express*. **28**, 17923 (2020).

7. W. D. Heiss, *J. Phys. A: Math. Theor.* **45**, 444016 (2012).

8. W. R. Sweeney, C. W. Hsu, S. Rotter, A. D. Stone, *Phys. Rev. Lett.* **122**, 093901 (2019).

9. Ş. K. Özdemir, S. Rotter, F. Nori, L. Yang, *Nat. Mater.* **18**, 783–798 (2019).

10. M.-A. Miri, A. Alù, *Science* **363**, 6422, (2019).

11. A. Regensburger, et al., *Nature* **488**, 167–171 (2012).

12. Z. Lin, et al., *Phys. Rev. Lett.* **106**, 213901 (2011).

13. L. Feng, Z. J. Wong, R.-M. Ma, Y. Wang, X. Zhang, *Science* **346**, 972–975 (2014).

14. J.-H. Park, et al., *Nat. Phys*. **16**, 462–468 (2020).

15. M. C. Rechtsman, *Nature*. **548**, 161–162 (2017).

16. H. Alaeian, J. A. Dionne, *Phys. Rev. A*. **89**, 033829 (2014).

17. X. Wang, X. Fang, D. Mao, Y. Jing, Y. Li, *Phys. Rev. Lett.* **123**, 214302 (2019).

18. M. Lawrence, et al., *Phys. Rev. Lett.* **113**, 093901 (2014).

19. S. H. Park, et al., *Nanophotonics* **9**, 1031–1039 (2020).

20. D. Lin, P. Fan, E. Hasman, M. Brongersma, *Science* **345**, 298–302 (2014).

21. G. Zheng, et al., *Nat. Nanotechn.* **10**, 308–312 (2015).

22. Q. Song, et al., *Nat. Commun.* **11**, 2651 (2020).

23. Q. Song, et al., *Sci. Adv.* **7**, eabe1112 (2021).

24. E. Plum, N. I. Zheludev, *Appl. Phys. Lett.* **106**, 221901 (2015).

25. X. Yang, M. Li, Y. Hou, J. Du, F. Gao, *Opt. Express* **27**, 6801 (2019).

26. A. Krasnok, et al., *Adv. Opt. Photon.* **11**, 892–951 (2019).

27. W. D. Heiss, H. L. Harney, *Eur. Phys. J. D*. **17**, 149–151 (2001).

28. M. Mcintyre, G. Cairns, *Geom Dedicata*. **46**, 149–159 (1993).

29. W. Luo, S. Xiao, Q. He, S. Sun, L. Zhou, *Adv. Opt. Mater.* **3**, 1102–1108 (2015).
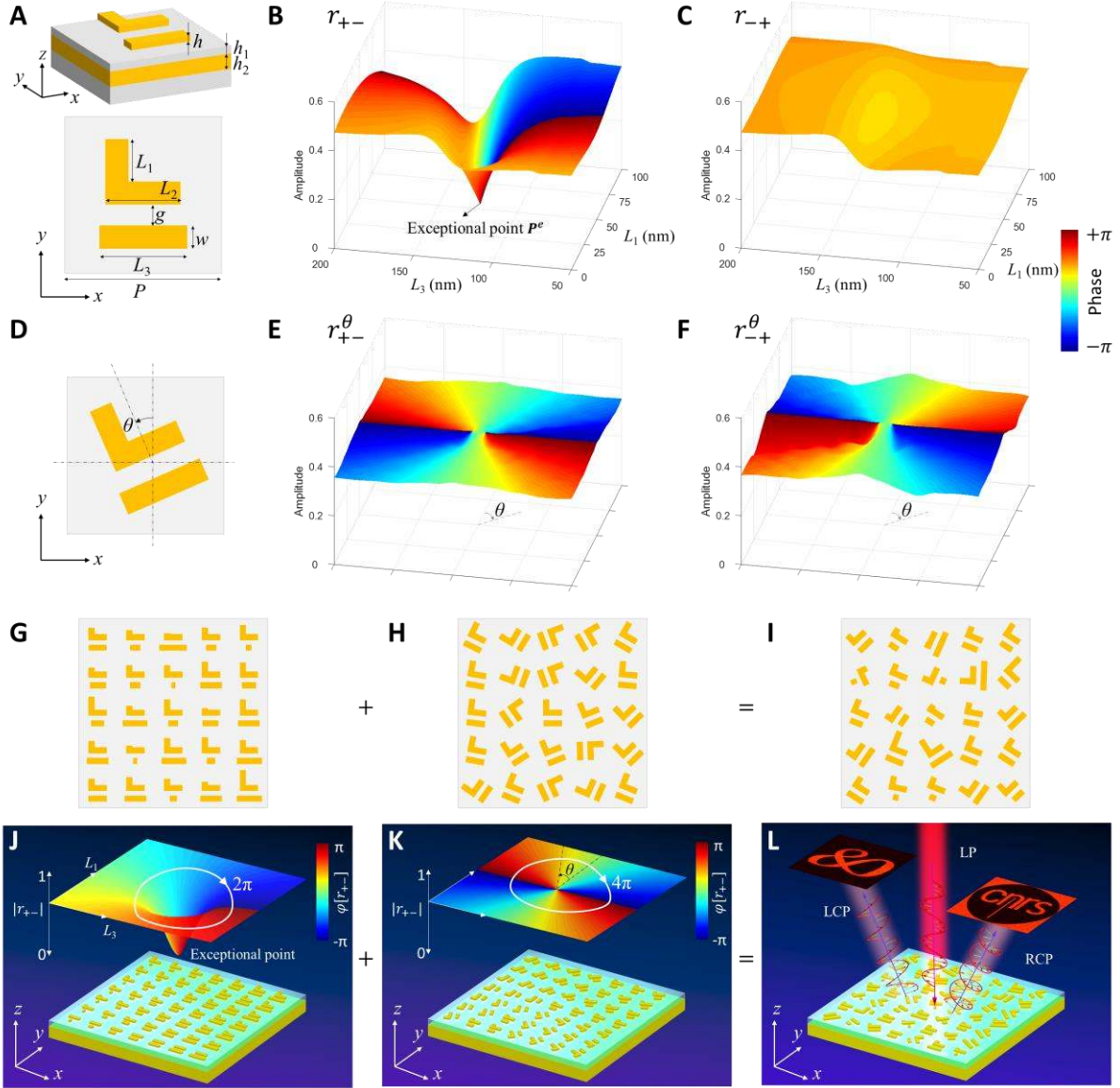
Acknowledgements

Supplementary Materials:

Materials and Methods

Figures S1-S14

Notes 1-5

Fig. 1. Design principle of the topological metasurface. (A) Perspective (top panel) and top (bottom panel) view of 2D chiral meta-atom design in reflection. The dimension is $L_2 = 140$ nm, $P = 300$ nm, $w = 50$ nm, $g = 70$ nm, $h = 30$ nm, $h_1 = 40$ nm, $h_2 = 150$ nm. (B) Simulated CP conversion coefficients r_{+-} and (C) r_{-+} in the parameter space covered by $L_1 \in [0, 100 \text{ nm}]$ and $L_3 \in [50 \text{ nm}, 200 \text{ nm}]$. An EP is obtained at $(L_1, L_3) = (52 \text{ nm}, 119 \text{ nm})$. A vortex phase profile for r_{+-} and a topological protected 2π phase accumulation is obtained by encircling the EP. (D) Top view of meta-atom with rotation angle of θ. (E) Simulated CP conversion coefficients r_{+-}^{θ} and (F) r_{-+}^{θ} with $\theta \in [0, 2\pi]$. In E and F, the original ET phase without rotation ($r_{\pm\mp}^0$) has been subtracted to display PB phase only. The z-axis in B, C, E and F represents the amplitude and the color scale represents the phase. The combination of (G) ET phase and (H) PB phase is designed to realize an ET+PB phase metasurface in (I). Schematics of the design implemented for combining the (J) ET and (K) PB phase control in (L) a single ET+PB phase metasurface, able to independently control the two CP beams.
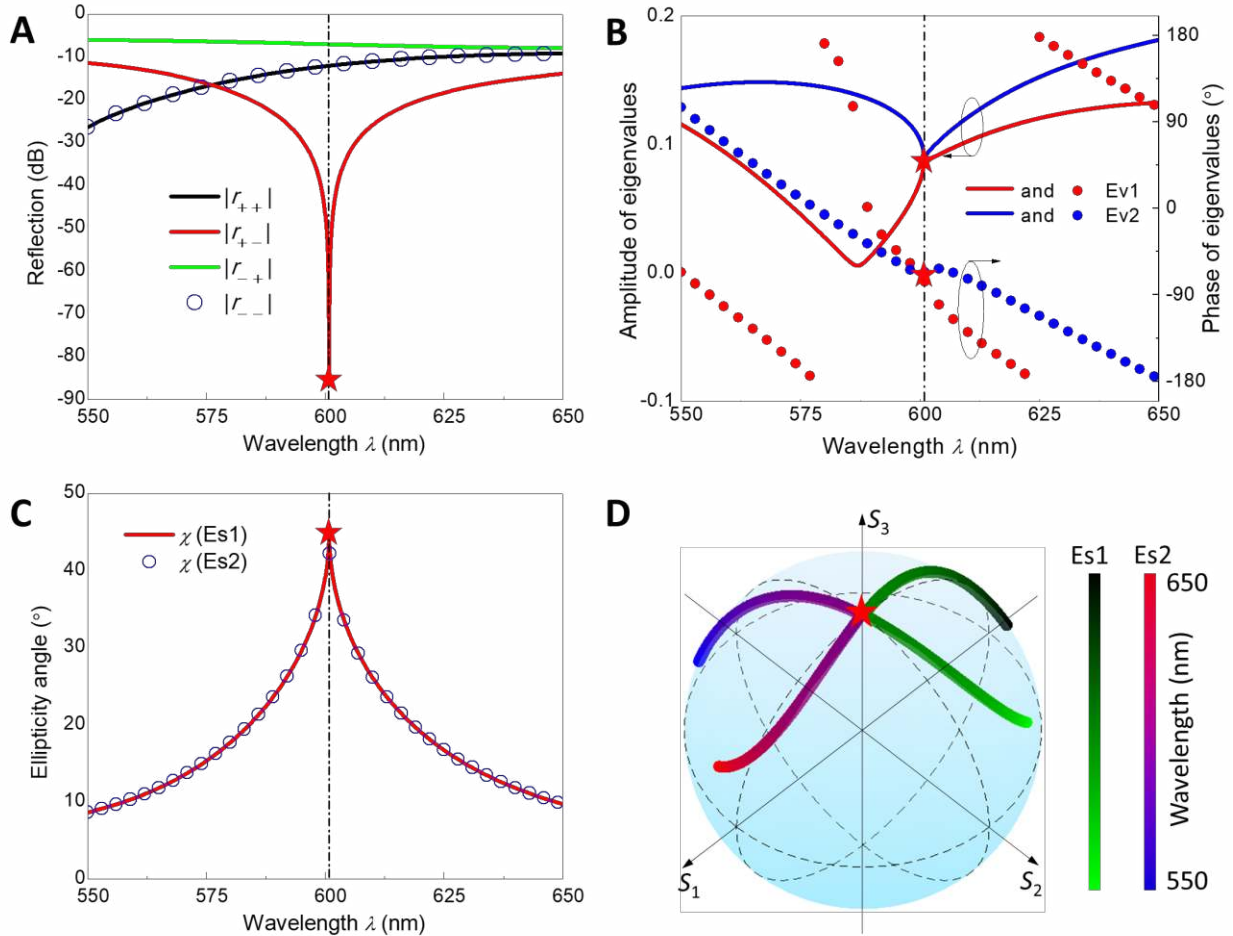
Fig. 2. Simulated reflection spectra and the corresponding eigenvalues and eigenstates. (A) Spectral dependence of the reflection matrix coefficients (in the circular basis). A singularity point, where $r_{+-} = 0$, is observed at $\lambda = 600$ nm. (B) Amplitude and phase of the reflection matrix eigenvalues. The two eigenvalues degenerate at $\lambda = 600$ nm. (C) Simulated ellipticity angle of the two eigenstates, which overlap and degenerate as RCP at $\lambda = 600$ nm. (D) Position of the eigenstates on the Poincaré sphere as a function of wavelength, which degenerate at $\lambda = 600$ nm. All the evidences prove that an EP is obtained at $\lambda = 600$ nm.
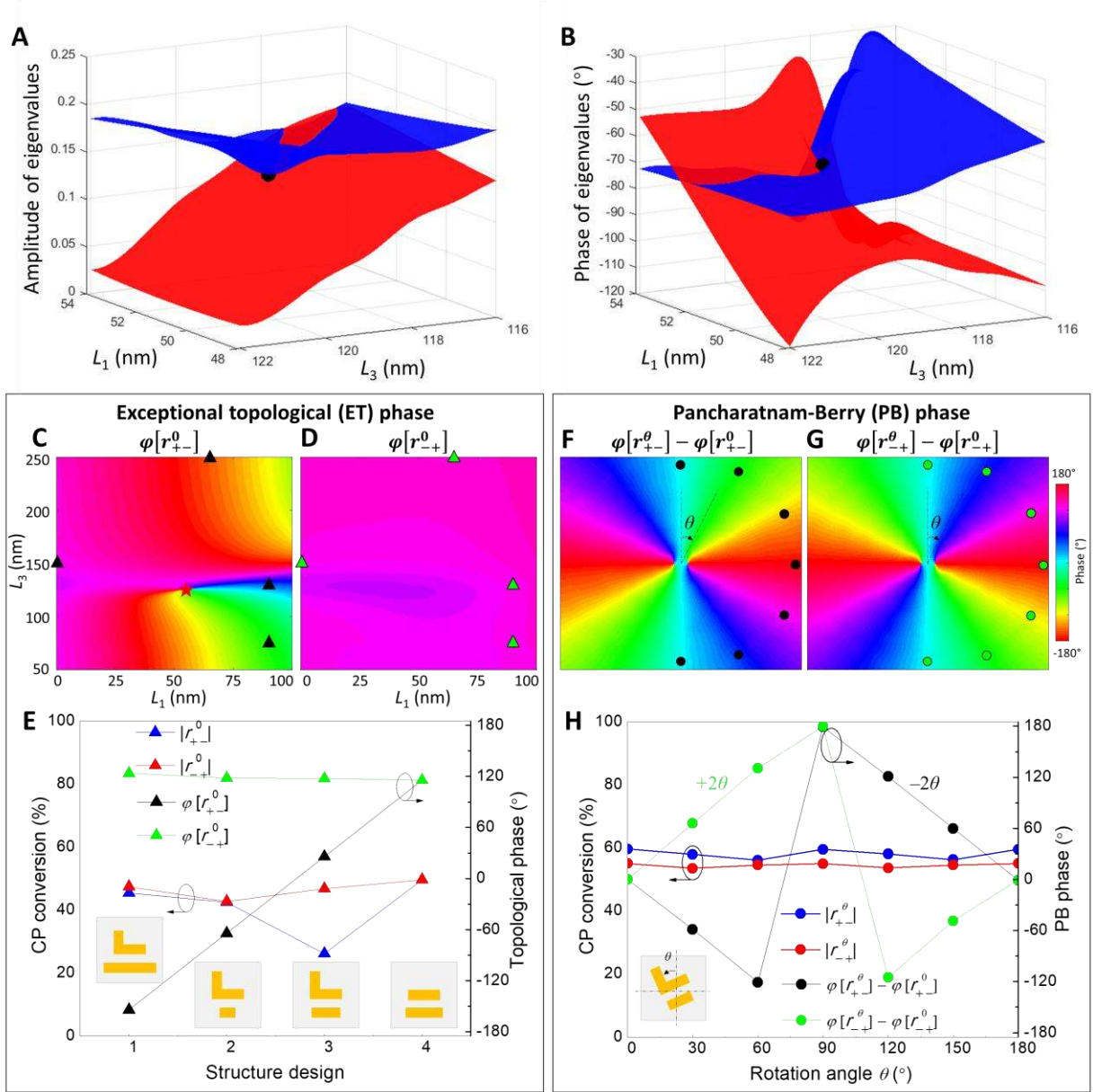
Fig. 3. Simulation results of the metasurface in the parameter space $R = (L_1, L_3)$. (A) Simulated amplitude and (B) phase of two eigenvalues at $\lambda = 600\,\text{nm}$. A self-intersecting Riemann surface profile is observed. The EP is highlighted as black dot, where two eigenvalues degenerate at $(L_1, L_3) = (52\,\text{nm}, 119\,\text{nm})$. (C) Simulated ET phase of r_{+-}^0 and (D) nearly constant phase of r_{-+}^0. (E) Four meta-atom designs are selected such that the ET phase interval is 90°, highlighted as triangles in C and D. The inset figures are four corresponding structure designs. (F) Simulated PB phase of r_{+-}^θ and (G) r_{-+}^θ, where the presented phase has been subtracted by the original phase of $r_{\pm\mp}^0$ without rotation to display PB phase only. (H) Seven rotated structures are presented with rotation angle from 0° to 180° stepped by 30°, highlighted as dots in F and G. (See more details in Supplementary fig. S11 and S14).

9
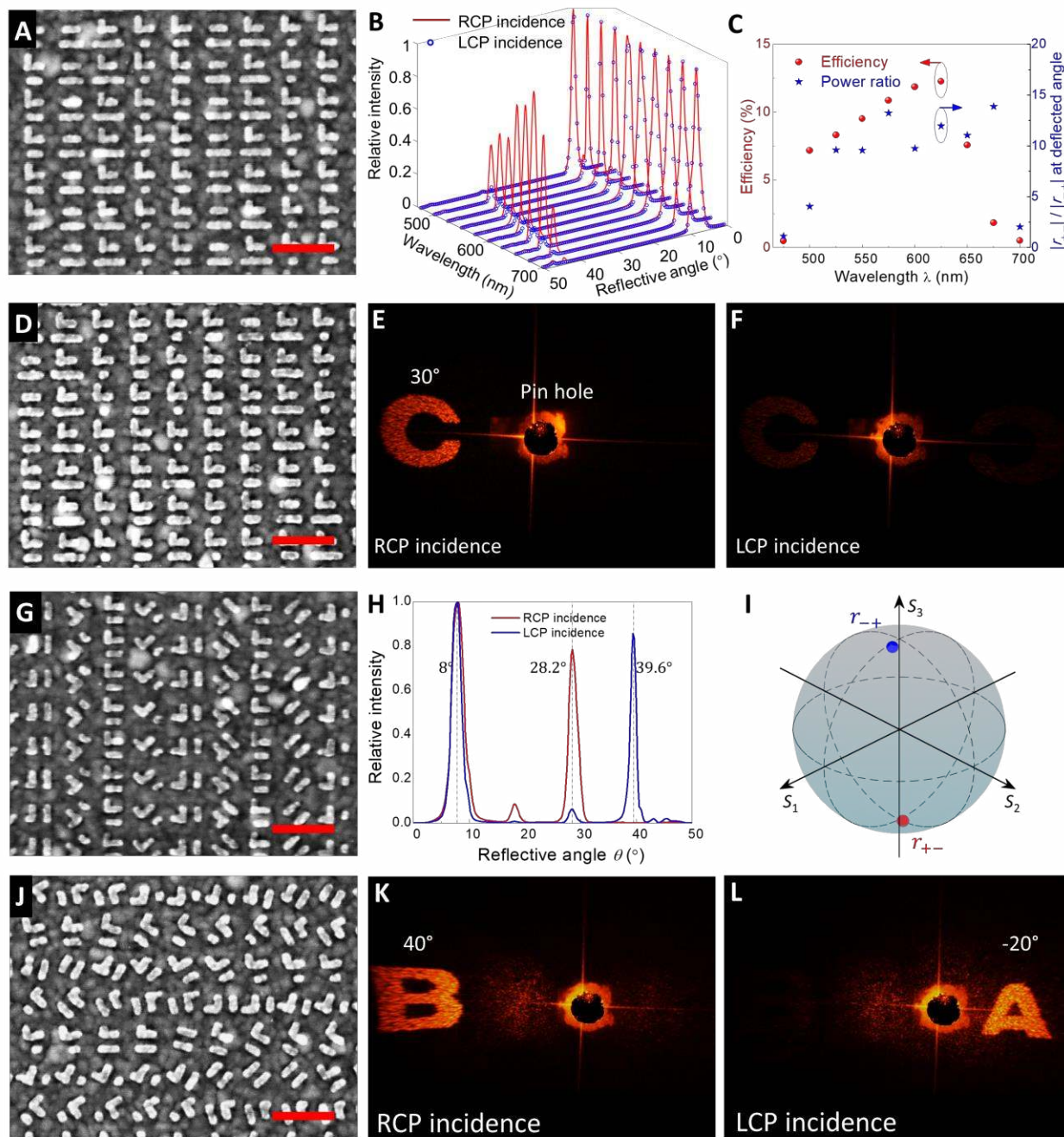
Fig. 4. Experimental results of the topological metasurface. (A) Fabricated nanostructures for the ET phase meta-deflector. (B) Measured far field power patterns for RCP (red solid curves) and LCP (blue dot curves) incidence on ET phase meta-deflector. The phase gradient between adjacent meta-atoms is designed as 90°. The first order of the CP converted beam r_{+-} is deflected from 34° to ~ 44° when the wavelength λ varies from 500 nm to ~ 675 nm, while the other CP converted beam of r_{-+} is undeflected (at the zero order of 8°). (C) Measured efficiency of the deflector (red dots) and measured power ratio of $|r_{+-}|/|r_{-+}|$ at the deflected angle (blue stars). (D) Fabricated nanostructures for an ET phase meta-hologram designed by encoding the holographic phase profile

into the deflector. (E) A holographic image of "C" for r_{+-} is displayed at the angle of 30º, (F) but no image appears for r_{-+}. (G) Fabricated nanostructures for an ET+PB phase meta-deflector. (H) Measured far field power patterns with RCP (red curve) and LCP (blue curve) incidence on ET+PB phase meta-deflector. The phase gradient between adjacent meta-atoms is designed as $60°$ and $90°$ respectively for r_{+-} and r_{-+}. (I) Poincaré sphere representation of the measured polarization of r_{+-} (red dot) and r_{-+} (blue dot) at the first deflected order. (J) Fabricated nanostructures for an ET+PB phase meta-hologram. (K) Holographic images of "B" for r_{+-} and (L) "A" for r_{-+} are displayed at the designed angle of $40°$ and $-20°$, respectively. All the curves in B and H are normalized with the zero order as unity. The operating wavelength in E, F, H, K and L is $\lambda = 600$ nm. The incident angles of the deflectors and holograms are $8°$ and $0°$, respectively. The scale bar in A, D, G, and J corresponds to 500 nm.

Science

AAAS

Supplementary Materials for

Plasmonic Topological Metasurface by Encircling an Exceptional Point

Authors: Qinghua Song[1], Mutasem Odeh[2], Jesús Zúñiga-Pérez[1], Boubacar Kanté[2], and Patrice Genevet[1]*

Affiliations:

[1]Université Côte d'Azur, CNRS, CRHEA, Rue Bernard Gregory, Sophia Antipolis 06560 Valbonne, France

[2]Depertment of Electrical Engineering and Computer Sciences, University of California, Berkeley, CA 94720, USA
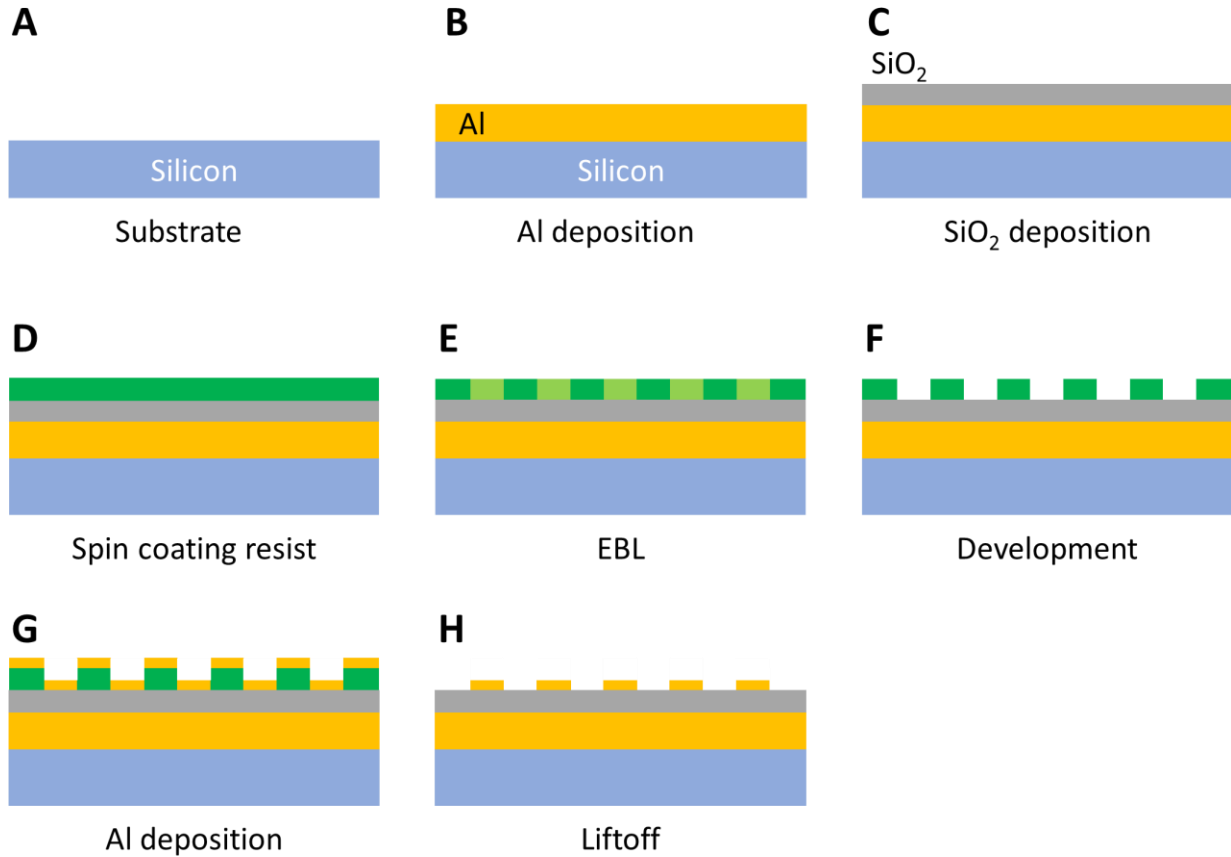
*Correspondence to: Patrice.Genevet@crhea.cnrs.fr.

This PDF file includes:

> Materials and Methods
> Figs. S1 to S14
> Notes 1-5

Materials and Methods

The fabrication processes and the measurement setup are shown in Fig. S1 and S2, respectively.

A

Silicon

Substrate

B

Al

Silicon

Al deposition

C

SiO₂

SiO₂ deposition

D

Spin coating resist

E

EBL

F

Development

G

Al deposition

H

Liftoff

Fig. S1. Plasmonic metasurface fabrication process. (A) Cleaning and dicing a silicon wafer into a 2 × 2 cm samples. (B) E-beam evaporation of 150 nm ground Al layer. (C) PECVD deposition of 40 nm SiO2 spacer layer. (D) Spin-coat and softback 220 nm PMMA-A4 e-beam resist. (E) 100keV e-beam lithography exposure of shape-corrected structure using BEAMER-GenISys software. (F) Cold-development using MBIK/IPA 1:3 for 2 minutes, followed by O2-plasma descumming process for 10 seconds. (G) E-beam evaporation of 30 nm Al device layer, and (H) lift-off process using room-temperature acetone solvent followed by 10-seconds sonication bath.
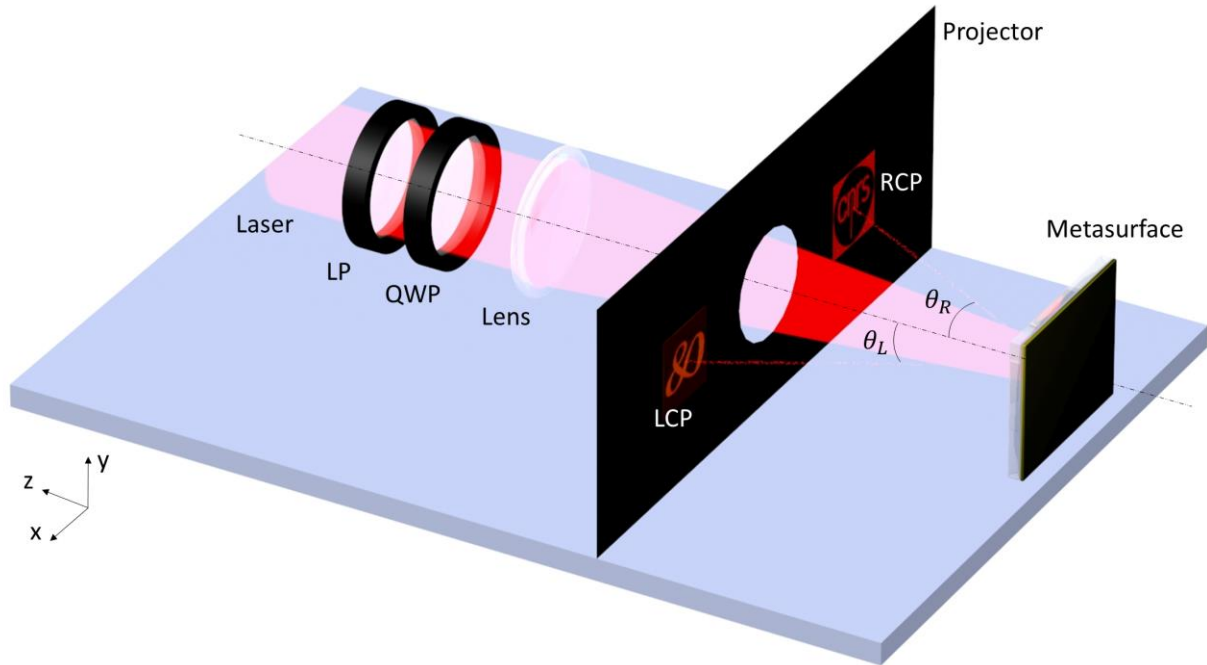
Fig. S2. Optical setup for the measurement of the meta-hologram. A laser beam at visible range propagates through a linear polarizer and quarter wavelength, so that a circular polarized light is obtained. Then the laser beam passes through a lens to weakly focus on the meta-hologram. The reflected holographic images are projected onto a projector with a hole in the center for the incident light passing through. LP: linear polarizer; QWP: quarter wave plate.

Supplementary Note 1: Phase accumulation by encircling a singularity point.

Consider an arbitrary complex number as a function of parameter $\boldsymbol{R}$,

$$f(\boldsymbol{R}) = Re[f(\boldsymbol{R})] + i\,Im[f(\boldsymbol{R})] \tag{S1}$$

where $Re[f(\boldsymbol{R})]$ and $Im[f(\boldsymbol{R})]$ represent the real and imaginary part of $f(\boldsymbol{R})$, respectively, $i^2 = -1$. The phase of complex number $f(\boldsymbol{R})$ can be described as

$$\phi[f(\boldsymbol{R})] = \angle f(\boldsymbol{R}) = \operatorname{atan}\frac{Im[f(\boldsymbol{R})]}{Re[f(\boldsymbol{R})]} \tag{S2}$$

When the parameter $\boldsymbol{R}$ varies continuously from point $\boldsymbol{P_1}$ to $\boldsymbol{P_2}$, the accumulated phase Φ along the path $\boldsymbol{P_1} \to \boldsymbol{P_2}$ in the complex plane $(Re[f(\boldsymbol{R})], Im[f(\boldsymbol{R})])$ as shown in fig. S3A is given by

$$\Phi = \int_{\phi[f(\boldsymbol{P_1})]}^{\phi[f(\boldsymbol{P_2})]} d\phi \tag{S3}$$

For any closed path l, if the origin is within the enclosed path l_1 as shown in fig. S3B, the winding number (28) of path l_1 around the origin $w = \frac{1}{2\pi}\oint d\phi = 1$. Therefore, the accumulated phase along the path l_1 is

$$\Phi = \oint d\phi = 2\pi \tag{S4}$$

However, if the origin is outside the enclosed path l_2 as shown in fig. S3C, the winding number is 0. Therefore, the accumulated phase along the path l_2 is

$$\Phi = \oint d\phi \neq 2\pi \tag{S5}$$

Assume that for a parameter space of $\boldsymbol{R}$, the complex number $f(\boldsymbol{R})$ vanishes at the parameter of $\boldsymbol{P^s}$, i.e., $f(\boldsymbol{P^s}) = Re[f(\boldsymbol{P^s})] + i\,Im[f(\boldsymbol{P^s})] = 0$. We will refer to such point of $\boldsymbol{P^s}$ ($f(\boldsymbol{P^s}) = 0$) as singularity point ($\boldsymbol{P^s}$) in this paper. For clarification, in the following text the variable $\boldsymbol{R}$ is defined in a two-dimensional parameter space $(\boldsymbol{R_1}, \boldsymbol{R_2})$, the complex number $f(\boldsymbol{R})$ is defined in the two-dimensional complex plane of $(Re[f(\boldsymbol{R})], Im[f(\boldsymbol{R})])$. When the parameter $\boldsymbol{R}$ is varied along a closed path in the parameter space of $(\boldsymbol{R_1}, \boldsymbol{R_2})$ as shown in fig. S4A and crosses the singularity point $\boldsymbol{P^s}$, the complex number $f(\boldsymbol{R})$ will pass through the origin in the complex plane $(Re[f(\boldsymbol{R})], Im[f(\boldsymbol{R})])$. Therefore, at least π phase can be accumulated as shown in fig. S4B.

Assume that at the vicinity of the singularity point P^s, the parameter R deviates from the previous path and encircles the singularity point P^s, as shown in fig. S4C. The complex number $f(R)$ will no longer pass through the origin in the complex plane of $(Re[f(R)], Im[f(R)])$. There are two possibilities for the evolution of the function $f(R)$, as shown in fig. S4D. Either it will encircle the origin, as shown by the red solid path (combined with the blue path), so that a full 2π phase can be accumulated, or the origin will be outside of the closed path as shown by the red dash path (combined with blue path), such that the accumulated phase is not 2π.
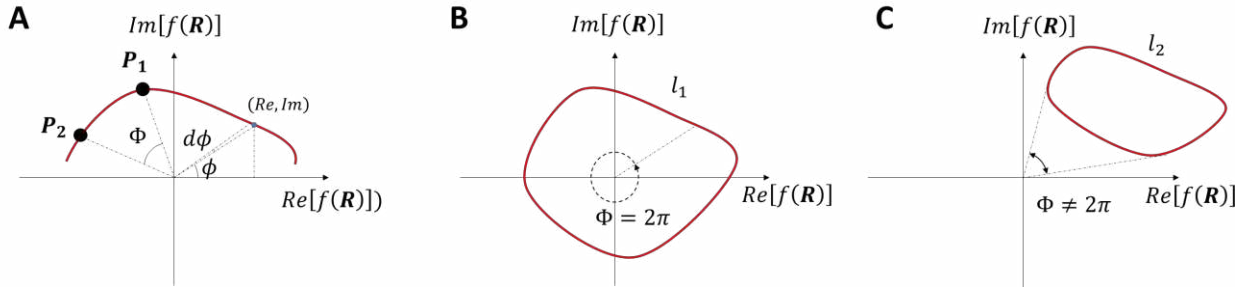
Fig. S3. Phase accumulation along a closed path in any parameter space R. (A) $Re[f(R)]$ and $Im[f(R)]$ represent the real and imaginary part of function $f(R)$, which are related to the parameter R. The phase of $f(R)$ is represented by ϕ. The phase accumulation along the path $P_1 \rightarrow P_2$ is Φ. (B) When the singularity point of $f(P^s) = 0$, i.e., the origin of the complex plane, is within the enclosed path l_1, a full 2π phase is accumulated along the path. (C) When the singularity point of $f(P^s) = 0$, i.e., the origin of the complex plane, is outside of the enclosed path l_2, the accumulated phase along the path is no longer 2π. The winding number of paths l_1 and l_2 along the origin is 1 and 0, respectively.
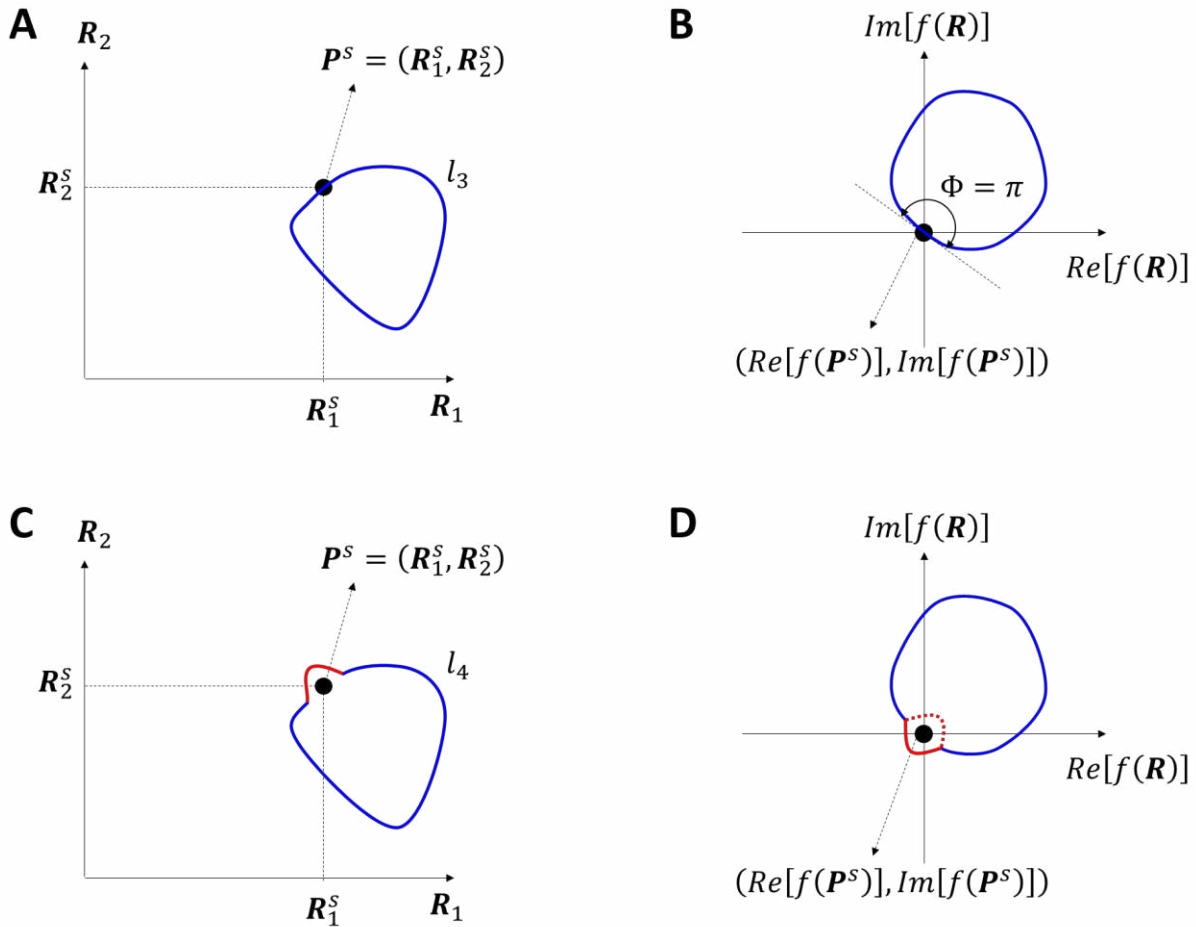
Fig. S4. Phase accumulation along a closed path in a two-dimensional parameter space $R = (R_1, R_2)$. (A) The singularity point $f(P^s) = 0$ exists at the parameter of $P^s = (R_1^s, R_2^s)$. The blue closed path l_3 crosses the singularity point. (B) The corresponding function $f(R) = Re[f(R)] + i\,Im[f(R)]$ crosses the origin in the complex plane. (C) At the vicinity of the singularity point, the parameter (R_1, R_2) deviates from the singularity point as shown in the red curve and encircles the singularity point by combining red and blue path l_4. (D) Two possibilities of evolution of the function $f(R)$ can be observed. The origin in the complex plane can be either within (red solid path) or out of (red dash path) the closed path of $f(R)$. For the red solid path together with blue path, a full 2π phase can be realized. For the red dash path together with the blue path, the phase accumulation is no longer 2π.

Supplementary Note 2: Robustness of the 2π phase accumulation: topological protection.

Here we consider the case of a closed path of $\boldsymbol{R} = (\boldsymbol{R_1}, \boldsymbol{R_2})$ that encircles the singularity point $\boldsymbol{P^s} = (\boldsymbol{R_1^s}, \boldsymbol{R_2^s})$, which implies that the closed path of $f(\boldsymbol{R})$ in the complex plane encircles the origin, as shown in the blue closed path of fig. S5A and S5B. The accumulated phase of $f(\boldsymbol{R})$ when encircling the singularity point $\boldsymbol{P^s}$ is 2π according to Eq. S4 as discussed in Note 1. Assume that the blue closed path is changed continuously to the red closed path without crossing the singularity point $\boldsymbol{P^s}$ as shown in fig. S5A. If the origin jumps outside of the function $f(\boldsymbol{R})$ as shown in fig. S5D, then there must exist an intermediate yellow path in parameter space $(\boldsymbol{R_1}, \boldsymbol{R_2})$ that imposes $f(\boldsymbol{R})$ to pass through the origin, as shown in fig. S5C. In this case, there must exist an additional singularity point of $\boldsymbol{P^{s\prime}}$, as shown by the yellow dot in fig. S5A, such that $f(\boldsymbol{P^{s\prime}}) = Re[f(\boldsymbol{P^{s\prime}})] + i\, Im[f(\boldsymbol{P^{s\prime}})] = 0$, as shown by the yellow dot in fig. S5C. Therefore, there must exist at least two singularity points $\boldsymbol{P^{s,s\prime}}$ such that the winding number of function $f(\boldsymbol{R})$ along the origin changes from 1 to 0 (from blue state in fig. S5B to red state in fig. S5D). In other words, a robust 2π phase accumulation is topologically protected by this singularity point unless the topology is broken by introducing another singularity point. In conclusion, if the following two conditions are satisfied a 2π phase accumulation is guaranteed for any closed path that encircles the singularity at point $\boldsymbol{P^s}$ in parameter space: (1) there exists only one singularity point $\boldsymbol{P^s}$ such that $f(\boldsymbol{P^s}) = 0$, (2) there exists one enclosed path that encircles the singularity point $\boldsymbol{P^s}$ such that the origin is within the path of $f(\boldsymbol{R})$ in the complex plane.
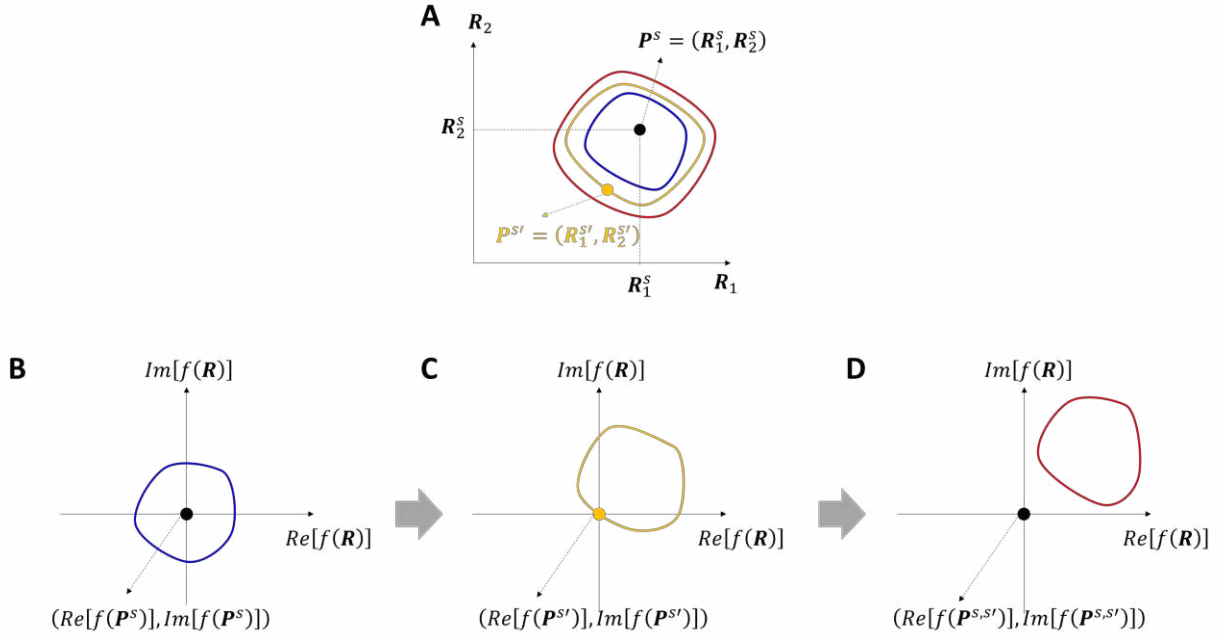
Fig. S5. Topology protection of 2π phase. (A) Three closed paths in the parameter space $R = (R_1, R_2)$. The singularity point exists at the parameter of $P^S = (R_1^S, R_2^S)$. The parameter is continuously changed from blue to yellow, and then to red path. All the three paths are encircling the singularity point of P^S. The corresponding path of $f(R)$ in the complex plane is shown in (B) blue, (C) yellow and (D) red paths. Assume the blue path of $f(R)$ is encircling the origin, i.e., a full 2π phase is accumulated along the closed path. When the path of $f(R)$ is changed from (B) to (D), there must exist an intermediate path as shown in (C), such that the function $f(R)$ passes through the origin. In other words, there must exist another singularity point of $P^{S\prime} = (R_1^{S\prime}, R_2^{S\prime})$ in the yellow path in (A). Therefore, the full 2π phase is topologically protected by R^S. By introducing another singularity point, the topology protection of 2π phase is broken.

Supplementary Note 3: General mathematic study of a planar chiral non-Hermitian matrix.

In this paper we only consider the metasurface with planar chiral anisotropic properties in the reflection regime, i.e.,

$$\begin{cases} r_{xx} \neq r_{yy} \\ r_{xy} = r_{yx} \end{cases} \tag{S6}$$

where r_{jk} is the reflection from k polarized input light to j polarized output light. $r_{xx} \neq r_{yy}$ due to the anisotropy, and $r_{xy} = r_{yx}$ due to the reciprocity. The reflection matrix can be described as,

$$\hat{r}(\mathbf{R}) = \begin{pmatrix} r_{xx}(\mathbf{R}) & r_{xy}(\mathbf{R}) \\ r_{yx}(\mathbf{R}) & r_{yy}(\mathbf{R}) \end{pmatrix} = \begin{pmatrix} a(\mathbf{R}) + ib(\mathbf{R}) & c(\mathbf{R}) + id(\mathbf{R}) \\ c(\mathbf{R}) + id(\mathbf{R}) & e(\mathbf{R}) + if(\mathbf{R}) \end{pmatrix} \tag{S7}$$

where a, b, c, d, e, f are arbitrary real values that are related to arbitrary system parameter $\mathbf{R}$. For simplicity, in some of the following discussions, we ignore the notation of $(\mathbf{R})$. Assume the eigenvalues and eigenstates of the matrix $\hat{r}$ is $\lambda_{1,2}$ and $|n_{1,2}\rangle$, i.e.,

$$\hat{r}|n_{1,2}\rangle = \lambda_{1,2}|n_{1,2}\rangle \tag{S8}$$

The eigenvalues can be derived as,

$$\lambda_{1,2} = \frac{(a+ib)+(e+if) \pm \sqrt{[(a+ib)-(e+if)]^2 + 4(c+id)^2}}{2} \tag{S9}$$

At the exceptional point of $\mathbf{P}^e$, the eigenvalues degenerate, i.e., the square root of $\lambda_{1,2}$ vanishes as,

$$\sqrt{\left[\left(a(\mathbf{P}^e)+ib(\mathbf{P}^e)\right)-\left(e(\mathbf{P}^e)+if(\mathbf{P}^e)\right)\right]^2 + 4\left(c(\mathbf{P}^e)+id(\mathbf{P}^e)\right)^2}$$

$$= \sqrt{[(a+ib)-(e+if)-2i(c+id)][(a+ib)-(e+if)+2i(c+id)]}$$

$$= \sqrt{[(a-e+2d)+i(b-f-2c)][(a-e-2d)+i(b-f+2c)]}$$

$$= 0 \tag{S10}$$

We then get

$$\begin{cases} a(\mathbf{P}^e) - e(\mathbf{P}^e) + 2d(\mathbf{P}^e) = 0 \\ b(\mathbf{P}^e) - f(\mathbf{P}^e) - 2c(\mathbf{P}^e) = 0 \end{cases} \tag{S11}$$

or

$$\begin{cases} a(\boldsymbol{P}^{e'}) - e(\boldsymbol{P}^{e'}) - 2d(\boldsymbol{P}^{e'}) = 0 \\ b(\boldsymbol{P}^{e'}) - f(\boldsymbol{P}^{e'}) + 2c(\boldsymbol{P}^{e'}) = 0 \end{cases} \tag{S12}$$

If the reflection matrix $\hat{r}(\boldsymbol{R})$ is Hermitian, i.e., $b(\boldsymbol{R}) = d(\boldsymbol{R}) = f(\boldsymbol{R}) = 0$, Eq. S11 and S12 coalesce as $a(\boldsymbol{P}^e) = e(\boldsymbol{P}^e)$, and $c(\boldsymbol{P}^e) = 0$. The eigenstates are $|n_1\rangle = \begin{pmatrix} 1 \\ 0 \end{pmatrix}$, $|n_1\rangle = \begin{pmatrix} 0 \\ 1 \end{pmatrix}$, which correspond to linearly-polarized orthogonal eigenstates.

5   However, if the reflection matrix $\hat{r}(\boldsymbol{R})$ is non-Hermitian, i.e., one of the imaginary parts b, d, f does not vanish, Eq. S11 and S12 give rise to two different cases. Consider the case of Eq. S11, i.e., $(a - e + 2d) + i(b - f - 2c) = 0$. According to Eq. S7-9 and S11, the degenerate eigenstates can be calculated as

$$|n_1\rangle = |n_2\rangle = |-\rangle = \begin{pmatrix} 1 \\ -i \end{pmatrix} \tag{S13}$$

10 which correspond to right circular polarization ($|-\rangle$), i.e., $\hat{r}(\boldsymbol{P}^e)|-\rangle = \lambda_{1,2}(\boldsymbol{P}^e)|-\rangle$. That means that when the incident light is pure RCP, the output light is also pure RCP, i.e., the CP conversion channel from RCP to LCP is blocked as,

$$r_{+-}(\boldsymbol{P}^e) = 0 \tag{S14}$$

where the subscript $+$ and $-$ represent LCP and RCP, respectively.

15 Since in the main text we will focus on experiments based on circularly-polarized beams, we will rewrite the matrix $\hat{r}$ in a circular polarization basis,

$$\hat{r} = \begin{pmatrix} r_{++} & r_{+-} \\ r_{-+} & r_{--} \end{pmatrix} = \frac{1}{2}\begin{pmatrix} r_{xx} + r_{yy} + i(r_{xy} - r_{yx}) & r_{xx} - r_{yy} - i(r_{xy} + r_{yx}) \\ r_{xx} - r_{yy} + i(r_{xy} + r_{yx}) & r_{xx} + r_{yy} - i(r_{xy} - r_{yx}) \end{pmatrix} \tag{S15}$$

If the reflection matrix $\hat{r}(\boldsymbol{R})$ is Hermitian, $r_{+-} = a - e - i2c$, and $r_{-+} = a - e + i2c$, the amplitude of r_{+-} always equals to r_{-+} (see fig. S6A). However, for Non-Hermitian reflection

20 matrix $\hat{r}(\boldsymbol{R})$, $r_{+-} = \frac{1}{2}(a - e + 2d) + \frac{i}{2}(b - f - 2c)$, and $r_{-+} = \frac{1}{2}(a - e - 2d) + \frac{i}{2}(b - f + 2c)$, we get unequal reflection for the two circular polarizations, i.e., $|r_{+-}| \neq |r_{-+}|$ (see fig. S6C). Consider the circular polarization conversion term r_{+-} and note that it is related to the system parameter $\boldsymbol{R}$ as,

$$r_{+-}(\boldsymbol{R}) = r_{xx}(\boldsymbol{R}) - r_{yy}(\boldsymbol{R}) - i\left(r_{xy}(\boldsymbol{R}) + r_{yx}(\boldsymbol{R})\right)$$

25
$$= \frac{1}{2}\left((a(\boldsymbol{R}) - e(\boldsymbol{R}) + 2d(\boldsymbol{R})) + i(b(\boldsymbol{R}) - f(\boldsymbol{R}) - 2c(\boldsymbol{R}))\right)$$

$$= Re[r_{+-}(\boldsymbol{R})] + i\, Im[r_{+-}(\boldsymbol{R})] \tag{S16}$$

According to Eq. S11, we get that at the exceptional point $\boldsymbol{P}^e$,

$$\begin{cases} Re[r_{+-}(\boldsymbol{P}^e)] = a(\boldsymbol{P}^e) - e(\boldsymbol{P}^e) + 2d(\boldsymbol{P}^e) = 0 \\ Im[r_{+-}(\boldsymbol{P}^e)] = b(\boldsymbol{P}^e) - f(\boldsymbol{P}^e) - 2c(\boldsymbol{P}^e) = 0 \end{cases} \tag{S17}$$

which is consistent with the analysis of Eq. S14. Therefore, the exceptional point $\boldsymbol{P}^e$ is a singularity point ($\boldsymbol{P}^s$ as discussed in Note 1-2) for $r_{+-}(\boldsymbol{R})$.

Similarly, if we consider the case of Eq. S12, the eigenstates degenerate as LCP ($|+\rangle$) at the exceptional point $\boldsymbol{P}^{e\prime}$,
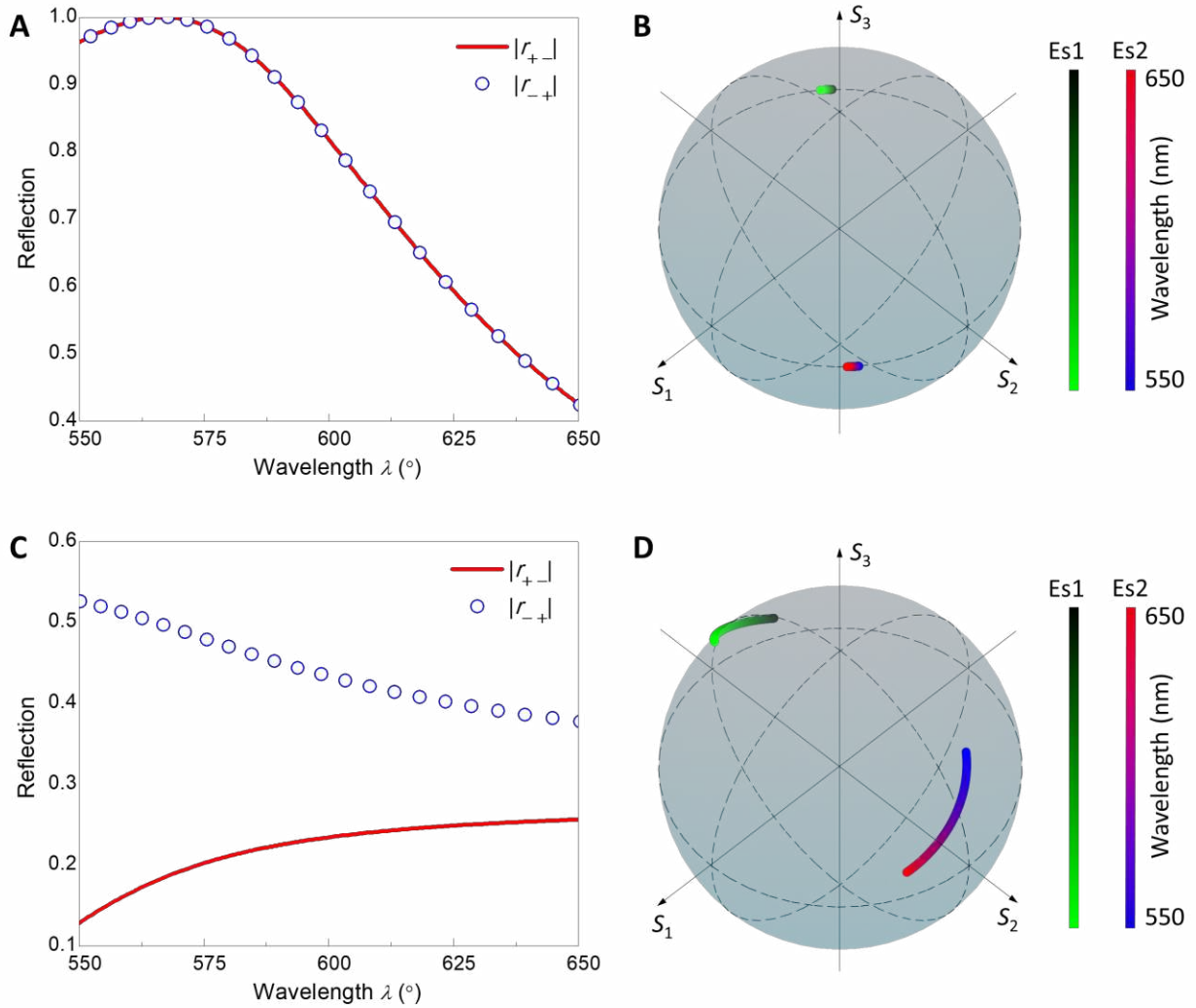
$$|n_1\rangle = |n_2\rangle = |+\rangle = \begin{pmatrix} 1 \\ i \end{pmatrix} \tag{S18}$$

We have,

$$r_{-+}(\boldsymbol{P}^{e\prime}) = 0 \tag{S19}$$

Therefore, the exceptional point $\boldsymbol{P}^{e\prime}$ is a singularity point ($\boldsymbol{P}^s$ as discussed in Note 1-2) for $r_{-+}(\boldsymbol{R})$.

Fig. S6. Comparison of lossless and lossy 2D chiral metasurfaces. (A) Simulated reflective CP conversion and (B) the corresponding eigenstates with perfect electrical conductor (PEC) structure. The amplitude of the two converted CP beams is the same. The two eigenstates are always linear polarized (on the equator of the Poincaré sphere). (C) Simulated reflective CP conversion and (D) the corresponding eigenstates with Al structure. The amplitude of the two converted CP beams becomes different. The two eigenstates become elliptical polarized with the same handedness (on the top sphere cap of the Poincaré sphere). The dimension of the structure in this case is $L_1 = 50$ nm, $L_2 = 140$ nm, $L_3 = 100$ nm, $P = 300$ nm, $w = 40$ nm, $g = 50$ nm, $h = 25$ nm, $h_1 = 40$ nm, $h_2 = 150$ nm. See more details of the discussion in Supplementary Note 3.
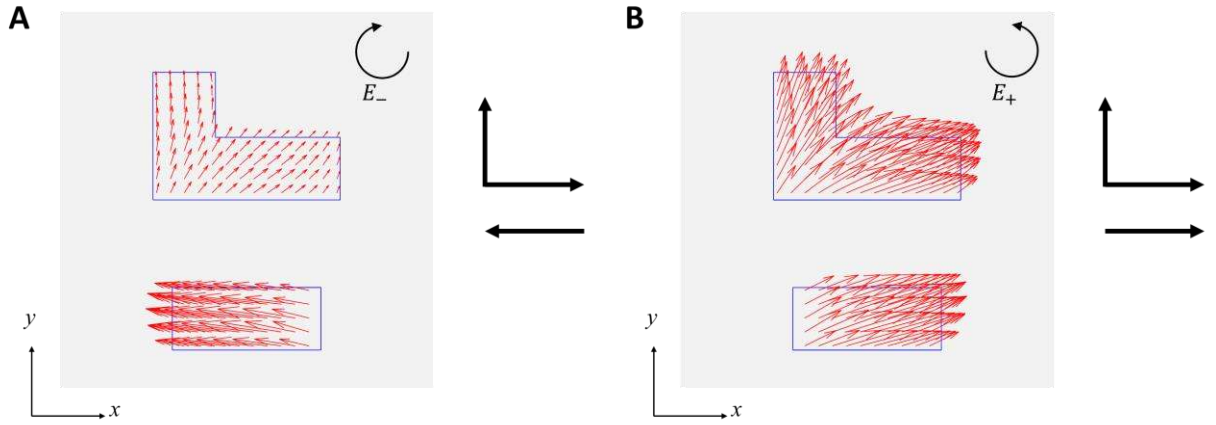
Fig. S7. Simulated surface current distribution at the exceptional point with (A) RCP and (B) LCP incidence. The two horizontal rods have bonding and anti-bonding current distribution under the two CP beam incidences. Changing the geometrical parameters of the meta-structure leads to destructive interference condition between the polarization converted from RCP to LCP and the unconverted fields of the reflected LCP, resulting in a zero reflection of r_{+-}, but leaving a non-zero reflection of r_{-+} due to the different response of the surface current.

Supplementary Note 4: Coupled-mode theory.

The metasurface consists of a "⌐" shape nanostructure stacked with an L shape rod and a straight rod in each meta-atom (see Fig. 1A in the main text). The structure can be modeled using coupled-mode theory inspired from the references of (*19-20*). The effective dipole moment of the structure is $p_{x,y} = \tilde{p}_{x,y}e^{i\omega t}$, which couples strongly to an incident radiation field $E_i = \tilde{E}_i e^{i\omega t}$ with a radiative coupling strength g_j. The resonant frequency and damping coefficient are ω_0 and γ, respectively. Assume the incident radiation is close to the resonance ($\delta = \omega - \omega_0 \approx 0$) and damping is small ($\gamma \ll \omega_0$), the dipole moments of the nanostructure in the coupled system are related to the incident electric fields through the polarizability matrix as,

$$\left[\begin{pmatrix} \delta_x + i\gamma_x & 0 \\ 0 & \delta_y + i\gamma_y \end{pmatrix} + \begin{pmatrix} G_{xx} & G_{xy} \\ G_{yx} & G_{yy} \end{pmatrix}\right] \begin{pmatrix} p_x \\ p_y \end{pmatrix} = \begin{pmatrix} g_x E_{ix} \\ g_y E_{iy} \end{pmatrix} \tag{S20}$$

where the coupling term G_{jk} is a summation of the *j*-oriented radiation fields formed by the *k*-oriented dipole moments, which satisfies the following condition $G_{xx} = G_{yy}$ due to the square lattice and $G_{xy} = G_{yx}$ due to the reciprocity. Therefore, the dipole moments can be retrieved as

$$\begin{pmatrix} p_x \\ p_y \end{pmatrix} = \begin{pmatrix} \delta_x + i\gamma_x + G_{xx} & G_{xy} \\ G_{xy} & \delta_y + i\gamma_y + G_{xx} \end{pmatrix}^{-1} \begin{pmatrix} g_x E_{ix} \\ g_y E_{iy} \end{pmatrix}$$

$$= \frac{1}{\det A} \begin{pmatrix} \delta_y + i\gamma_y + G_{xx} & -G_{xy} \\ -G_{xy} & \delta_x + i\gamma_x + G_{xx} \end{pmatrix} \begin{pmatrix} g_x E_{ix} \\ g_y E_{iy} \end{pmatrix} \tag{S21}$$

where $\det A$ is the determinant of matrix $A = \begin{pmatrix} \delta_x + i\gamma_x + G_{xx} & G_{xy} \\ G_{xy} & \delta_y + i\gamma_y + G_{xx} \end{pmatrix}$. The reflective field can be obtained by superposing the incident field reflected back from the ground mirror and the field radiated in the forward direction due to the oscillating dipoles, given by $\frac{i\omega\eta_0}{2a^2}(g_x p_x, g_y p_y)$, where $\eta_0 = \sqrt{\mu_0/\varepsilon_0}$ is the free space impedance and a is the lattice constant. Therefore, the reflective field is,

$$\begin{pmatrix} E_{ox} \\ E_{oy} \end{pmatrix} = \hat{r} \begin{pmatrix} E_{ix} \\ E_{iy} \end{pmatrix}$$

$$= Q \begin{pmatrix} g_x^2(\delta_y + i\gamma_y + G_{xx}) & -g_x g_y G_{xy} \\ -g_x g_y G_{xy} & g_y^2(\delta_x + i\gamma_x + G_{xx}) \end{pmatrix} \begin{pmatrix} E_{ix} \\ E_{iy} \end{pmatrix} - \begin{pmatrix} E_{ix} \\ E_{iy} \end{pmatrix} \tag{S22}$$

where $E_{ox,y}$ indicates the output field in *x*- and *y*- polarization, $Q = \frac{i\omega\eta_0}{2a^2}\frac{1}{\det A}$. Therefore, the reflection matrix is

$$\hat{r} = Q \begin{pmatrix} g_x^2(\delta_y + i\gamma_y + G_{xx}) & -g_x g_y G_{xy} \\ -g_x g_y G_{xy} & g_y^2(\delta_x + i\gamma_x + G_{xx}) \end{pmatrix} - \hat{I}$$
$$= \begin{pmatrix} a + ib & c + id \\ c + id & e + if \end{pmatrix} \tag{S23}$$

where

$$\begin{cases} a = Qg_x^2(\delta_y + G_{xx}) - 1 = Qg_x^2(\omega - \omega_y + G_{xx}) - 1 \\ \quad\quad b = g_x^2 \gamma_y \\ \quad\quad c = -g_x g_y G_{xy} \\ \quad\quad d = 0 \\ e = Qg_y^2(\delta_x + G_{xx}) - 1 = Qg_y^2(\omega - \omega_x + G_{xx}) - 1 \\ \quad\quad f = g_y^2 \gamma_x \end{cases} \tag{S24}$$

According to Eq. S16, S23 and S24, we can get the real and imaginary part of the polarization converted part $r_{+-}(\mathbf{R})$ as

$$\begin{cases} Re[r_{+-}] = \dfrac{Q}{2}\left(g_x^2(\omega - \omega_y + G_{xx}) - g_y^2(\omega - \omega_x + G_{xx})\right) \\ \quad Im[r_{+-}] = \dfrac{1}{2}\left(g_x^2 \gamma_y - g_y^2 \gamma_x + 2g_x g_y G_{xy}\right) \end{cases} \tag{S25}$$

If there is only one resonance in either x or y polarization, let's say in x polarization, i.e., $\omega_x \approx \omega$, $\omega_y \approx 0$, the real part of $r_{+-}(\mathbf{R})$ becomes $Re[r_{+-}] \approx \frac{Q}{2}\left(g_x^2(\omega + G_{xx}) - g_y^2 G_{xx}\right) = \frac{Q}{2}g_x^2\omega + \frac{Q}{2}G_{xx}(g_x^2 - g_y^2) \approx \frac{Q}{2}g_x^2\omega > 0$. Therefore, the maximum phase of $r_{+-}(\mathbf{R})$ is π as shown in fig. S8A. However, if there are two resonances in both x and y polarization, i.e., $\omega_x \approx \omega$, $\omega_y \approx \omega$, the real part of $r_{+-}(\mathbf{R})$ around the resonance frequency becomes $Re[r_{+-}] \approx \frac{1}{2}QG_{xx}(g_x^2 - g_y^2)$, which can be either positive or negative by rationally controlling g_x and g_y. As a result, a full 2π phase can be obtained as shown in fig. S8B.

Figure S9 shows the simulated results of the reflection spectrum with linear polarized incidence. When L_1 is fixed as $L_1 = 70$ nm and the length of L_3 is controlled from 90 nm to 150 nm as shown in fig. S9A, the resonance dips in the y-polarization (r_{yy}) keep constant as shown in the dash line because the effective length of the nanostructure in y-direction keeps constant. However, since the effective length of the nanostructure in x-direction in increasing, the resonance dips of r_{xx} red shift as shown in the solid line. It can be seen that there is a cross of the two resonances in x- and y- polarization, so that the coupling of the two polarization enables a full 2π phase change of $r_{+-}(\mathbf{R})$ as discussed before. Likewise, if L_3 is fixed as $L_3 = 100$ nm and the

length of L_1 is controlled from 50 nm to 80 nm, a resonance dip crossing is also observed as shown in fig. S9B. Therefore, by controlling L_1 and L_3, it is able to realize a full 2π phase change of $r_{+-}(\boldsymbol{R})$.

The simulated results of real and imaginary part of $r_{+-}(\boldsymbol{R})$ in the parameter space covered by $L_1 \in [48\text{ nm}, 58\text{ nm}]$ and $L_3 \in [112\text{ nm}, 122\text{ nm}]$ are shown in fig. S10. The yellow and blue areas represent the positive and negative sign of r_{+-}. An exceptional point is obtained as indicated in the red star, where the eigenstates degenerate as RCP ($|-\rangle$), such that $r_{+-} = 0$. At the vicinity of the exceptional point, when L_1 increases, the resonance frequency ω_y decreases while ω_x keeps constant around ω as shown in fig. S9B, so that the real part of r_{+-}: $Re[r_{+-}] = \frac{1}{2}\Big(Qg_x^2(\omega - \omega_y +$ $G_{xx}) - Qg_y^2(\omega - \omega_x + G_{xx})\Big) \approx \frac{1}{2}Qg_x^2(\omega - \omega_y)$ increases, resulting in a positive value of $Re[r_{+-}]$ with larger L_1 as shown in fig. S10A, and vice-versa. When L_3 increases, g_x, G_{xy} and γ_x are increasing, the imaginary part of r_{+-}: $Im[r_{+-}] = \frac{1}{2}\big(g_x^2\gamma_y - g_y^2\gamma_x + 2g_xg_yG_{xy}\big)$ increases. Because the power index of the first term (g_x^2) and third term (g_xG_{xy}) is twice compared to the second term (γ_x), such that the increasing of $g_x^2\gamma_y + 2g_xg_yG_{xy}$ is more dramatic than the decreasing of $g_y^2\gamma_x$. Thus, a positive value of $Im[r_{+-}]$ is obtained with larger L_3 as shown in fig. S10B, and vice-versa. Therefore, a full 2π phase of r_{+-} is obtained by encircling the EP in the parameter space of (L_1, L_3) at the vicinity of EP. As discussed in Note 2, such 2π phase is topologically protected with arbitrary closed path that is encircling the EP, even if we extend the parameter space of (L_1, L_3) to $L_1 \in (0\text{ nm}, 100\text{ nm})$, $L_3 \in (50\text{ nm}, 250\text{ nm})$ as shown in Fig. 1B and 3C in the main text and fig. S11, as long as there is only one EP in the interested parameter space.
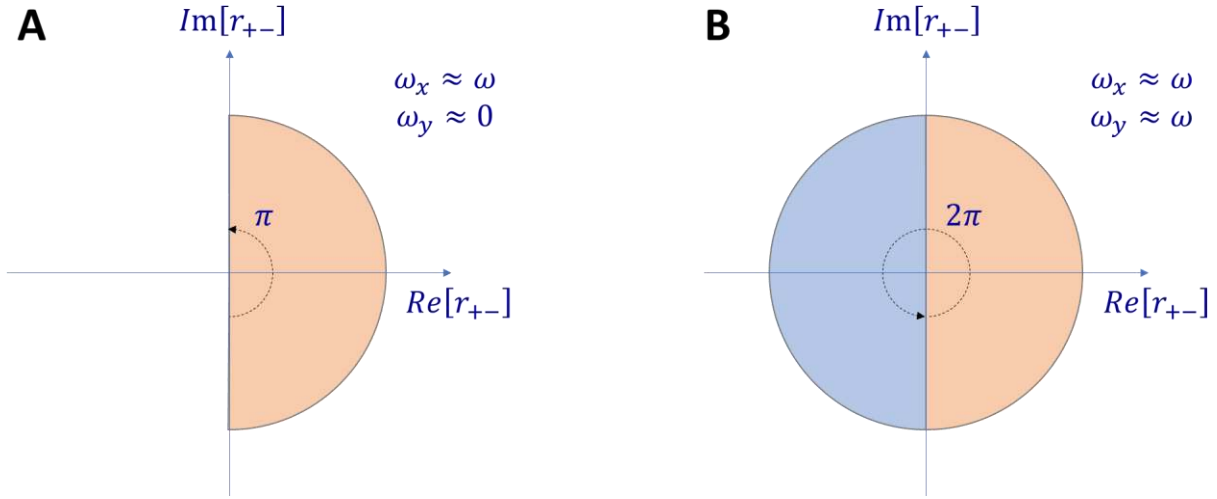
Fig. S8. Phase accumulation of r_{+-} from coupled-mode theory. (A) When there is only one resonance in x-polarization ($\omega_x \approx \omega$, $\omega_y \approx 0$), the maximum phase accumulation of r_{+-} is π. (B) Together with the other resonance in y-polarization ($\omega_x \approx \omega$, $\omega_y \approx \omega$), a full 2π phase can be achieved.
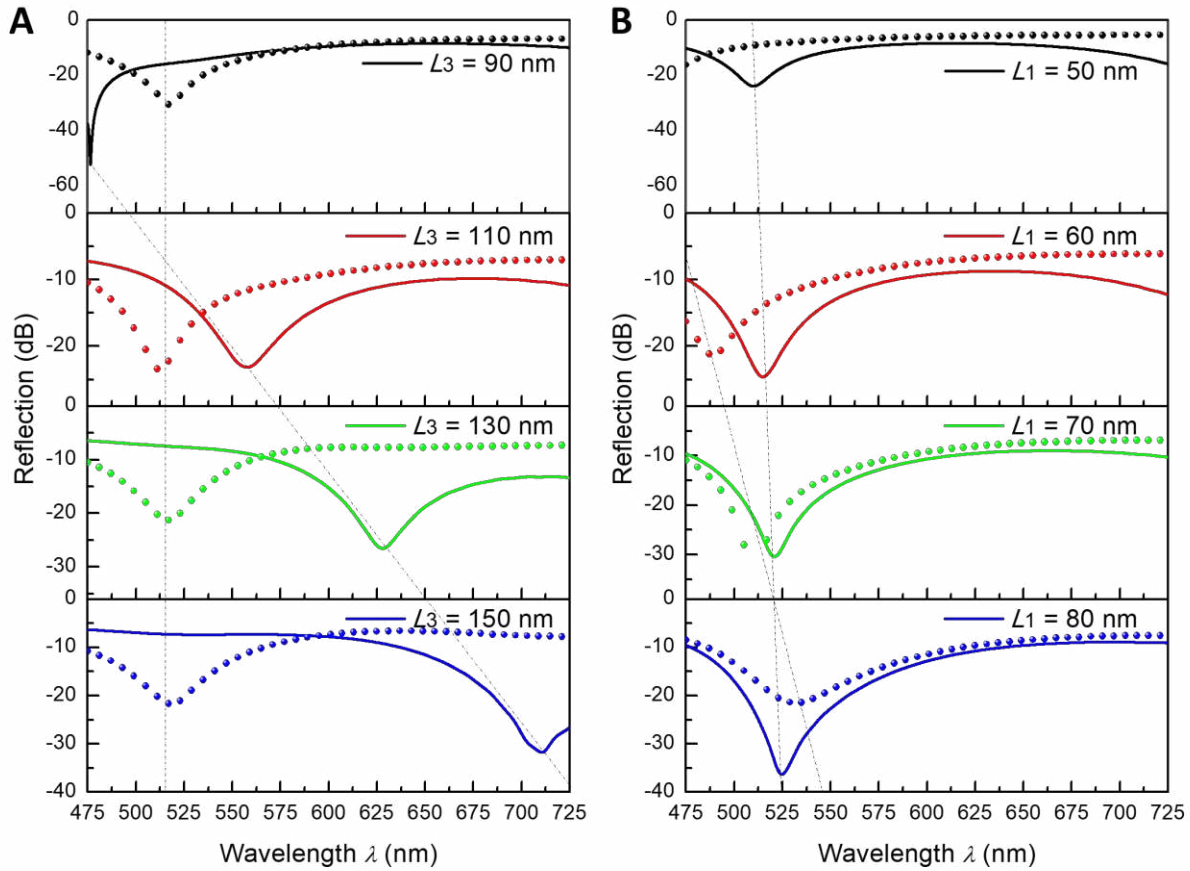
Fig. S9. Simulated results of the reflection spectrum with linear polarization incidence. Solid and dot lines represent r_{xx} and r_{yy}, respectively. (A) Simulated results with L_1 fixed as 70 nm and L_3 is changed from 90 nm to 150 nm. The effective length of the meta-atom in the y-direction is fixed, such that the resonance dips of r_{yy} keep constant. While the effective length of the meta-atom in the x-direction is increasing, resulting in a red shift of the resonance dips of r_{xx}. (B) Simulated results with L_3 fixed as 100 nm and L_1 is changed from 50 nm to 80 nm. The effective length of the meta-atom in the x-direction is fixed, such that the resonance dips of r_{xx} keep constant. While the effective length of the meta-atom in the y-direction is increasing, resulting in a red shift of the resonance dips of r_{yy}. It can be observed that the two resonance dips in x- and y-directions have a cross as shown in the two dash lines. Therefore, by changing L_1 and L_3, it is possible to couple the two resonances in x- and y- directions to obtain a full 2π phase of r_{+-}.
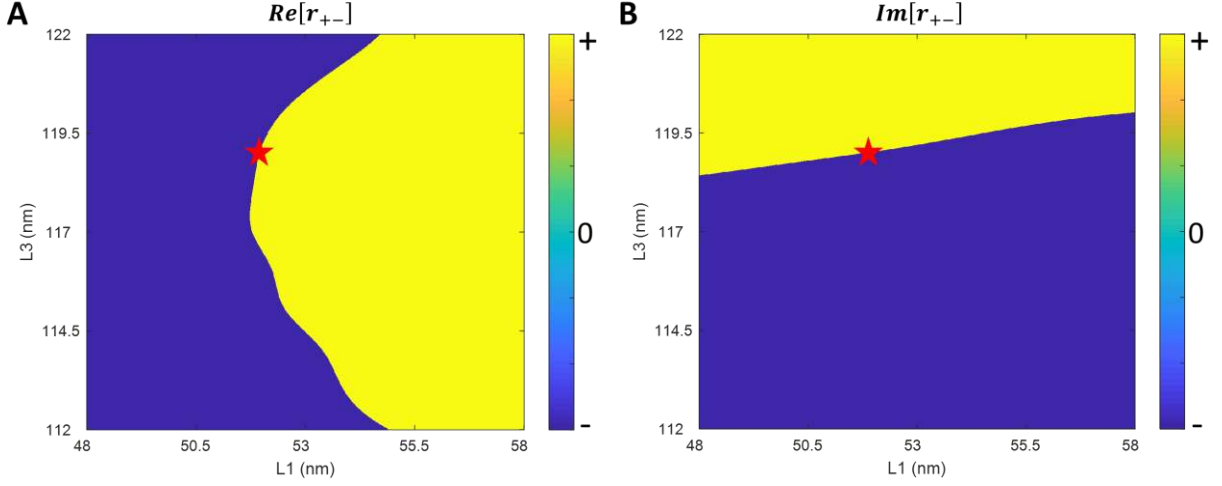
Fig. S10. Simulated results of r_{+-} in the parameter space covered by $L_1 \in [48\,\text{nm}, 58\,\text{nm}]$ and $L_3 \in [112\,\text{nm}, 122\,\text{nm}]$. The yellow and blue colors represent the positive and negative sign of r_{+-}, respectively. The red dots represent the exceptional point, where both real and imaginary parts of r_{+-} vanish. (A) Real and (B) imaginary part of r_{+-}. At the vicinity of the EP ($Re[r_{+-}] = Im[r_{+-}] = 0$), for the real part of r_{+-}, when L_1 increases, the resonance frequency ω_y decreases, so that $Re[r_{+-}]$ increases, resulting in a positive value of $Re[r_{+-}]$, and vice-versa. For the imaginary part of r_{+-}, when L_3 increases, both g_x and G_{xy} increases, so that $Im[r_{+-}]$ increases, resulting in a positive value of $Im[r_{+-}]$, and vice-versa. Therefore, a full 2π phase of r_{+-} is obtained by encircling the EP.
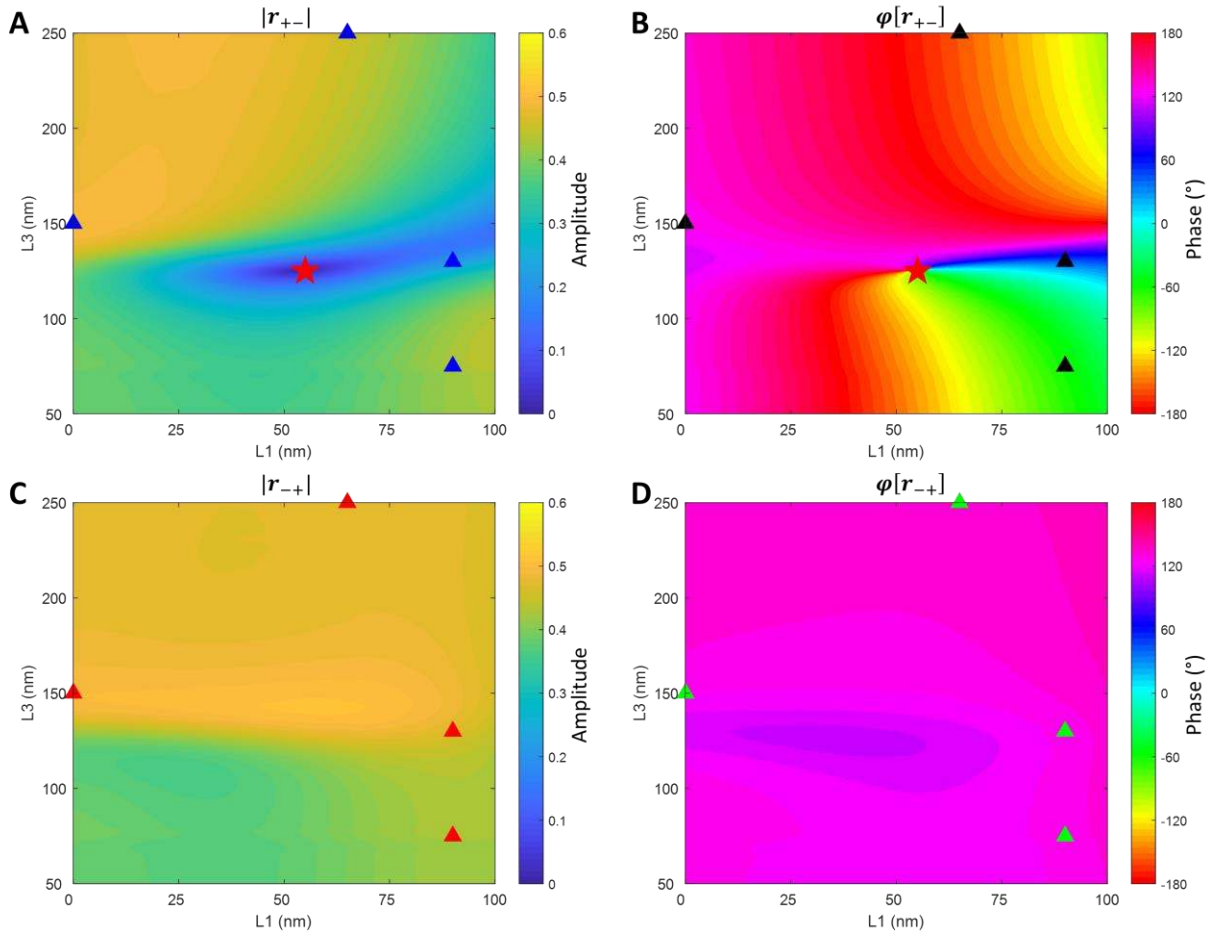
Fig. S11. Simulated reflection map of topological metasurface at the wavelength of 600 nm.
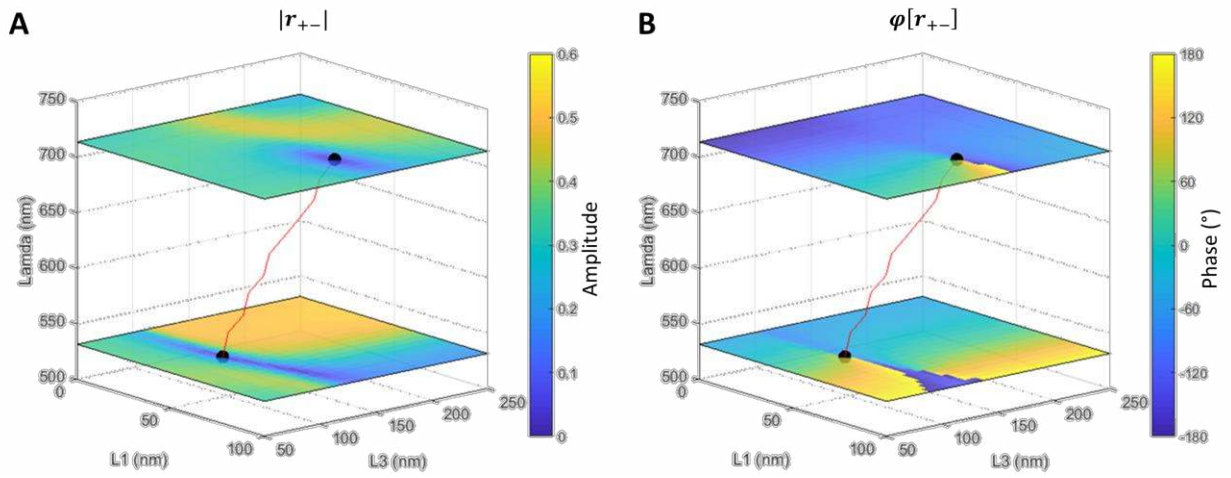(A) Amplitude and (B) phase of r_{+-}. (C) Amplitude and (D) phase of r_{-+} in the parameter space covered by $L_1 \in [0, 100 \text{ nm}]$ and $L_3 \in [50 \text{ nm}, 250 \text{ nm}]$. The EP occurs at the parameter of $(L_1, L_3) = (52 \text{ nm}, 119 \text{ nm})$ as highlighted in red stars, where the amplitude of r_{+-} vanishes and a vortex phase profile of $\varphi[r_{+-}]$ is observed. A full 2π phase accumulation can be obtained by encircling the EP. The corresponding 3D surf maps of $r_{\pm\mp}$ are shown in Fig. 1B-1C in the main text. Figure S11B and S11D are the same with Fig. 3C and 3D in the main text. The four triangles represent four metasurface design with an ET phase interval of 90º. The amplitude and phase values of these four designs are shown in Fig. 3G in the main text.
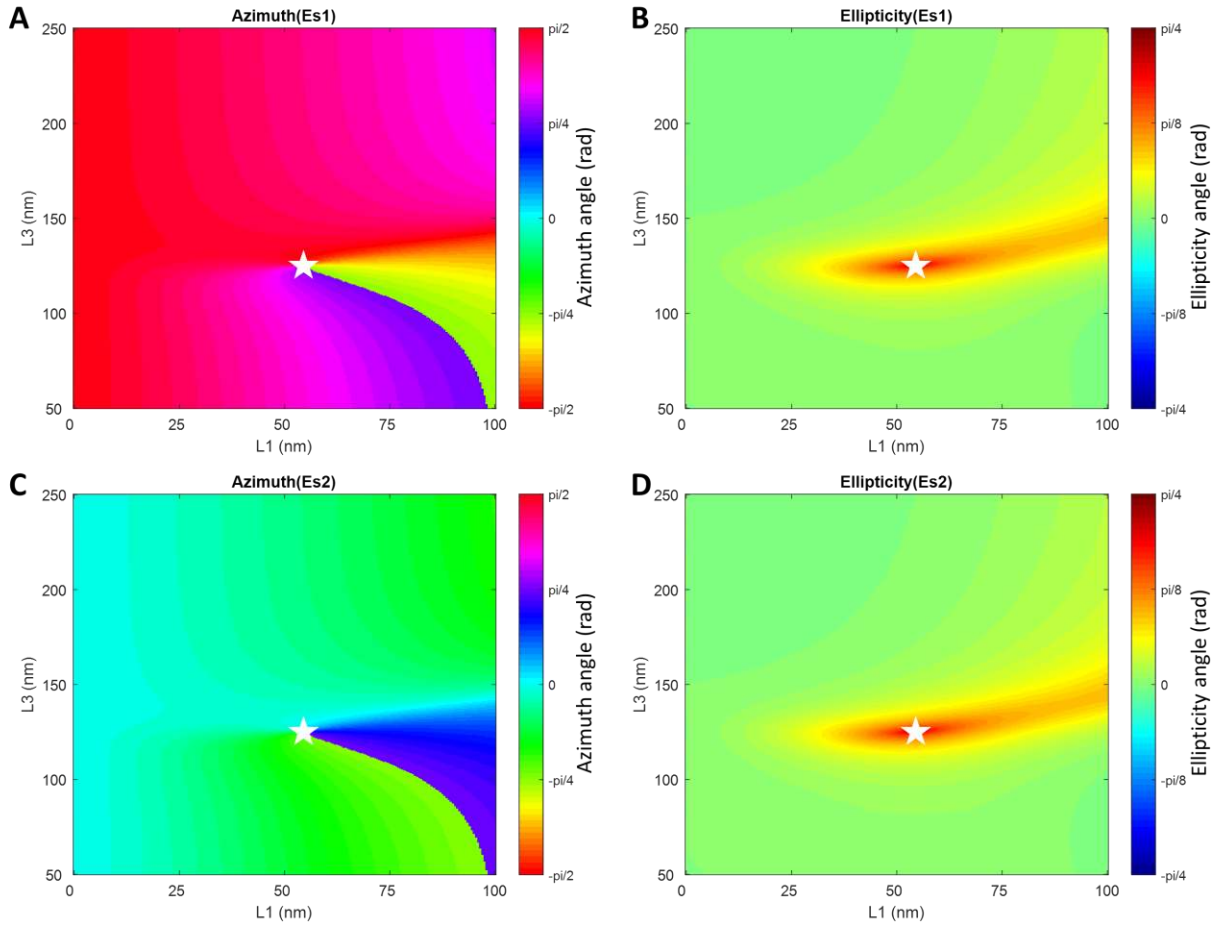
Fig. S12. Eigenstates of reflection matrix at the wavelength of 600 nm. (A) Azimuth and (B) ellipticity angle of the first eigenstate. (C) Azimuth and (D) ellipticity angle of the second eigenstate in the parameter space covered by $L_1 \in [0, 100 \text{ nm}]$ and $L_3 \in [50 \text{ nm}, 250 \text{ nm}]$. The red stars represent the EPs where both eigenstates coalesce as RCP.

Fig. S13. Exceptional point trajectory as a function of wavelength in the parameter space of (L_1, L_2). (A) Amplitude and (B) phase of r_{+-}. The red lines represent the trajectory of the EP.

Supplementary Note 5: Combination with Pancharatnam-Berry (PB) phase by rotating the metasurface.

Assume the metasurface is rotated with an angle of θ relative to the reference coordinate system $\{x, y\}$ (see Fig. 1D in the main text), the reflection matrix in the circular-polarization representation can be expressed as,

$$\hat{r}^{\theta}(\boldsymbol{R}) = \begin{pmatrix} r_{++}^{\theta}(\boldsymbol{R}) & r_{+-}^{\theta}(\boldsymbol{R}) \\ r_{-+}^{\theta}(\boldsymbol{R}) & r_{--}^{\theta}(\boldsymbol{R}) \end{pmatrix} = M(-\theta)\hat{r}(\boldsymbol{R})M(\theta) \tag{S26}$$

By employing the Pauli matrices notation $\{\sigma_1, \sigma_2, \sigma_3\}$ and the identity matrix $\hat{I}$ (29), the $2\times$ 2 rotation matrix M is equal to $e^{i\theta\sigma_3}$, which can be expanded by Taylor series as $M(\theta) = \cos\theta\,\hat{I} + i\sin\theta\,\sigma_3$. Therefore, the reflection matrix can be described as following,

$$\hat{r}^{\theta}(\boldsymbol{R}) = \frac{1}{2}(r_{xx} + r_{yy})\hat{I} + \frac{i}{2}(r_{xy} - r_{yx})\sigma_3$$

$$+ \frac{1}{2}(r_{xx} - r_{yy})(e^{-i2\theta}\sigma_+ + e^{i2\theta}\sigma_-) + \frac{i}{2}(r_{xy} + r_{yx})(-e^{-i2\theta}\sigma_+ + e^{i2\theta}\sigma_-) \tag{S27}$$

where two spin-flip operators $\sigma_\pm = \frac{\sigma_1 \pm i\sigma_2}{2}$ satisfy $\sigma_\pm|\pm\rangle = 0$ and $\sigma_\pm|\mp\rangle = |\pm\rangle$, with $|\pm\rangle$ denoting LCP and RCP, respectively. When the metasurface is illuminated with RCP ($|-\rangle$), the reflection is

$$r^{\theta}(\boldsymbol{R}) = \hat{r}^{\theta}(\boldsymbol{R})|-\rangle = \frac{1}{2}(r_{xx} + r_{yy})\hat{I}|-\rangle + \frac{i}{2}(r_{xy} - r_{yx})\sigma_3|-\rangle$$

$$+ \frac{1}{2}(r_{xx} - r_{yy})e^{-i2\theta}|+\rangle - \frac{i}{2}(r_{xy} + r_{yx})e^{-i2\theta}|+\rangle \tag{S28}$$

where the first two terms represent the CP unconverted part and the last two terms represent the CP converted part, i.e.,

$$r_{+-}^{\theta}(\boldsymbol{R}) = \frac{(r_{xx} - r_{yy}) - i(r_{xy} + r_{yx})}{2}e^{-i2\theta} = r_{+-}^{0}(\boldsymbol{R})e^{-i2\theta} \tag{S29}$$

where $r_{+-}^{0}(\boldsymbol{R})$ represents the original ET phase without rotation as shown in Eq. S15. Therefore, a geometric phase of -2θ is applied into r_{+-} when the metasurface is rotated with an angle of θ. Similarly, when the metasurface is illuminated with LCP ($|+\rangle$), the CP converted part can be expressed as,

$$r_{-+}^{\theta}(\boldsymbol{R}) = \frac{(r_{xx} - r_{yy}) + i(r_{xy} + r_{yx})}{2}e^{i2\theta} = r_{-+}^{0}(\boldsymbol{R})e^{i2\theta} \tag{S30}$$

Thus, an opposite geometric phase of 2θ is applied into r_{-+}.

In conclusion, the reflective CP conversion is,

$$r_{\pm\mp}^{\theta}(R) = r_{\pm\mp}^{0}(R)e^{\mp i2\theta} = \left|r_{\pm\mp}^{0}(R)\right|e^{i\varphi\left[r_{\pm\mp}^{0}(R)\right]}e^{\mp i2\theta} \tag{S31}$$
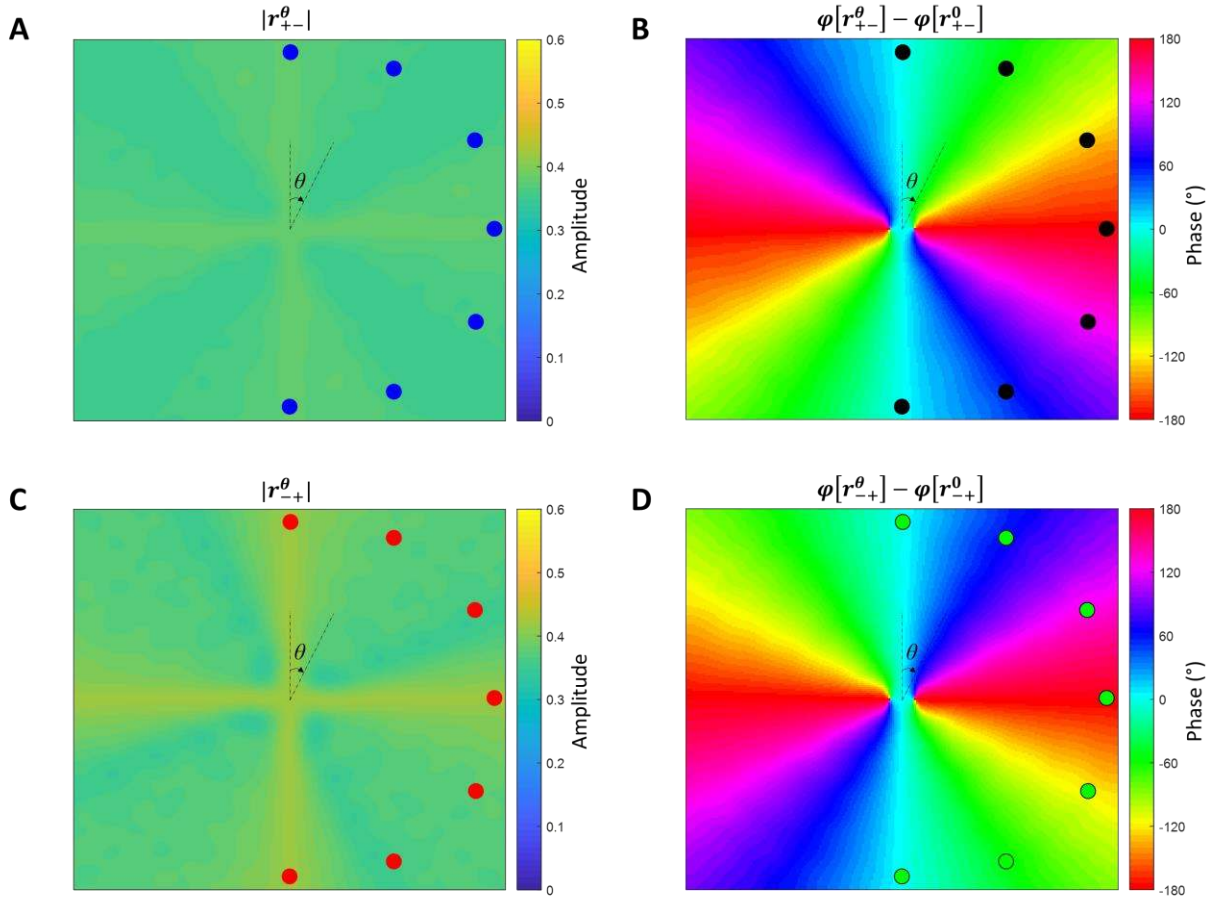
where $|x|$ and $\varphi[x]$ represent the amplitude and phase of complex value x. Therefore, the overall phase of the CP conversion term with rotation angle of θ is the combination of the original ET phase without rotation and a geometric phase as,

$$\varphi\left[r_{\pm\mp}^{\theta}(R)\right] = \varphi\left[r_{\pm\mp}^{0}(R)\right] \mp 2\theta \tag{S32}$$

The simulated reflection 3D surf maps of the rotated metasurface with (L_1, L_2) fixed at (80 nm, 95 nm) when the rotation angle of the meta-atom is changed from 0 to 2π are shown in Fig. 1E and 1F in the main text. The corresponding 2D color maps are shown in fig. S14. The simulated PB phase is also presented in Fig. 3F and 3G in the main text. An opposite of PB phase of $\mp 2\theta$ is shown in $r_{\pm\mp}$.

In the real metasurface design, assuming the desired phase profile for $r_{\pm\mp}^{\theta}$ is $\varphi_d\left[r_{\pm\mp}^{\theta}\right]$, we can derive the necessary ET phase of r_{+-}^{0} and the necessary rotation angles corresponding to the additional PB phase, as given by Eq. S32 (where we have taken into account that $\varphi[r_{-+}^{0}] = 0$),

$$\begin{cases} \varphi[r_{+-}^{0}] = \varphi_d\left[r_{+-}^{\theta}\right] + \varphi_d\left[r_{-+}^{\theta}\right] \\ \quad \theta = \dfrac{\varphi_d\left[r_{-+}^{\theta}\right]}{2} \end{cases} \tag{S33}$$

Fig. S14. Simulated reflection color maps of rotated metasurface at the wavelength of 600 nm with (L_1, L_2) fixed at (80 nm, 95 nm) when the rotation angle of the meta-atom is changed from 0 to 2π. (A) Amplitude and (B) phase of r_{+-}. (C) Amplitude and (D) phase of r_{-+} with rotation angle of θ ranging from 0 to 2π. The represented phase of $r_{\pm\mp}^{\theta}$ in B and D has been subtracted by the phase of $r_{\pm\mp}^{0}$ with zero rotation angle, such that a pure PB phase can be observed. An opposite topology of vortex phase profile can be seen, which is intrinsically different from the topological phase by encircling the EP as shown in fig. S11. The corresponding 3D surf maps of $r_{\pm\mp}^{\theta}$ are shown in Fig. 1E-1F in the main text. Figure S14B and S14D are the same with Fig. 3E and 3F in the main text. The seven dots represent seven rotation angles from 0º to 180º with a step of 30º. The amplitude and phase values of these seven designs are shown in Fig. 3H in the main text.